Built on LDRD Laboratory Directed Research and Development

SAND2016-XXXXR
LDRD PROJECT NUMBER: 16-0757
LDRD PROJECT TITLE: Advanced Imaging Algorithms for Radiation Imaging Systems
PROJECT TEAM MEMBERS: Peter Marleau, Kyle Polack, and Sara Pozzi

ABSTRACT:

Radiation-imaging devices are important to the nuclear security and safeguards communities due to their ability to detect and localize radioactive sources. Because of their low natural background, difficulty to shield, and unique association with SNM, fast-neutron imaging provides a promising means for the detection of SNM. To make these R&D systems useful for end-user applications, robust reconstruction and analysis algorithms must be developed that provide detailed information on the location, energy spectrum, and intervening material. To date, deconvolution, match filtering, and MLEM have been demonstrated. However, the information provided is limited to an approximate location of the source.

The intent of this work was to develop the algorithms that will bring the analysis from qualitative images to quantitative attributes of objects containing SNM. The first step to achieving this was to develop an in-depth understanding of the intrinsic errors associated with the deconvolution and MLEM algorithms. Toward that end, significant effort went into developing bootstrap methods for estimating statistical uncertainties and experimentally validating them.

These methods were exercised on University of Michigan's Dual Particle Imager to demonstrate that simultaneous reconstruction of fast neutron and gamma-ray images and spectra can be made quantitative. The results were then used to evaluate potential sources of systematic uncertainty.

INTRODUCTION:

This University Campus Executive project has focused on advancing imaging algorithms to be used with radiation imaging systems with the goal of enabling their eventual use as tools for the quantitative characterization and detection of special nuclear material. This effort has culminated in the PhD thesis of Kyle Polack who has successfully defended and will be joining Sandia National Laboratories staff in FY17. Most of the remainder of this report are excerpts from his dissertation. For a more complete description, the reader is directed to his thesis work[1].

Measurements of photon and neutron signatures are an effective method for detecting and characterizing SNM. Both signatures provide unique information about an SNM sample and can be used to infer information about any shielding material that may be present. While there are

[1] K. Polack, "A Maximum-Likelihood Approach for Localizing and Characterizing Special Nuclear Material with a Dual-Particle Imager", a dissertation submitted in partial fulfillment of the requirements for the degree of Doctor of Philosophy in the University of Michigan. 2016.

.

many photon-emitting sources in the environment, neutron emitting sources are less likely to be present, and are therefore more likely to signify the presence of SNM.

Photon signatures from SNM appear as both fixed-energy decay lines and broad distributions associated with nuclear fission[2]. Photons are also frequently created through the interaction of neutrons with other material in the surrounding environment. Neutron signatures appear with a variety of energy distributions, the most notable of which is the Watt distribution, which is representative of neutrons originating from fission[2]. Also notable are the energy distributions associated with (α, n) reactions, which contribute to the neutrons emitted by SNM in oxide form. (α, n) distributions are also associated with ^{9}Be(α, n) sources, which often contain plutonium and can therefore be classified as SNM [2,3]. The specifics of the key photon and neutron signatures will be explained in greater detail as they become relevant to the measurements presented in this work.

It is possible to reduce the detectability of both photon and neutron signatures through the use of shielding. However, each particle interacts in a different, distinct manner depending on the material. Photons will preferentially interact with high-Z materials, and can therefore be effectively shielded by materials such as lead and tungsten[3]. Neutrons are more effectively moderated by low-Z materials, and can therefore be shielded by hydrogenous materials such as polyethylene. As a result, it is more difficult to shield a source from detection if a measurement system is sensitive to both photon and neutron signatures.

The amount of information contained in the photon and neutron signatures of SNM have led to the development of many measurement systems relevant to the non-proliferation and treaty verification fields [2, 4]. Some devices focus solely on count rates, while other devices aim to take advantage of the information contained in energy spectra and particle multiplicity distributions[2].

Radiation imaging systems have a distinct advantage over more traditional systems in that they are able to provide localized information. While a particle counter can tell you if something is present and a spectrometer can tell you what is present, an imaging system can tell you what is present and where. Of course, it is also possible to obtain localized information with non-imaging systems. However, this requires actively measuring each location of interest with a well collimated detector, which can quickly become impractical if source locations are unknown. Imaging systems, on the other hand, can collect information from many locations simultaneously, producing a single snapshot of the entire radiation field.

---

[2] Los Alamos National Laboratory, *Passive Nondestructive Assay of Nuclear Materials*. 1991
[3] G. F. Knoll, *Radiation Detection and Measurement*, 4th ed. John Wiley & Sons, 2010
[4] D. Henzlova, R. Kouzes, R. McElroy, P. Peerani, M. Aspinall, K. Baird, A. Bakel, M. Borella, M. Bourne, L. Bourva, F. Cave, R. Chandra, D. Chernikova, S. Croft, G. Dermody, A. Dougan, J. Ely, E. Fanchini, P. Finocchiaro, V. Gavron, M. Kureta, K. D. Ianakiev, K. Ishiyama, T. Lee, C. Martin, K. McKinny, H. O. Menlove, C. Orton, A. Pappalardo, B. Pedersen, D. Peranteau, R. Plenteda, S. Pozzi, M. Schear, M. Seya, E. Siciliano, S. Stave, L. Sun, M. T. Swinhoe, H. Tagziria, S. Vaccaro, J. Takamine, A.-L. Weber, T. Yamaguchi, and H. Zhu, "Current Status of Helium-3 Alternative Technologies for Nuclear Safeguards," Los Alamos, NM (United States), Dec. 2015.
.

Many applications will benefit from the ability to obtain localized information of a radiation field. Search applications derive an obvious benefit from radiation imaging as the source location is inherently unknown. The International Atomic Energy Agency (IAEA) has publicly stated its interest in imaging systems for a variety of safeguards applications[5]. Emergency responders may wish to investigate and characterize a suspicious object without having to physically enter or open the object. Finally, arms-control inspectors can use imaging techniques to individually characterize several objects in close proximity to one another such as multiple reentry vehicles contained within a single warhead[6] or numerous plutonium pits stored in dismantlement containers[7].

Numerous imaging systems have been (and are currently being) developed to aid in the endeavors listed above. These systems leverage various imaging modalities including coded aperture[8,9,10], particle scattering [6,11,12,13], and time-encoding imaging[14,15]. Many of these imaging systems were developed to detect a single particle type of interest, either photons or neutrons. However, the benefits afforded by sensitivity to both neutrons and photons have led to the development of new systems[16,17,18] and new capabilities[19]. Realizing the full potential of these

[5] International Atomic Energy Agency, "RFP 26070-EO Specifications for Gamma Imaging System," 2015
[6] K. P. Ziock, C. J. Hailey, T. B. Gosnell, J. H. Lupton, and F. A. Harrison, "A gamma-ray imager for arms control," *IEEE Trans. Nucl. Sci.*, vol. 39, no. 4, pp. 1046–1050, 1992.
[7] National Nuclear Security Administration Office of Nonproliferation and Arms Control and Misistry of Defence Atomic Weapons Establishment, "Joint U.S.-U.K. Report on Technical Cooperation for Arms Control," 2015
[8] S. Zelakiewicz, R. Hoctor, A. Ivan, W. Ross, E. Nieters, W. Smith, D. McDevitt, M. Wittbrodt, and B. Milbrath, "SORIS—A standoff radiation imaging system," *Nucl. Instruments Methods Phys. Res. Sect. A Accel. Spectrometers, Detect. Assoc. Equip.*, vol. 652, no. 1, pp. 5–9, Oct. 2011
[9] P. Marleau, J. Brennan, E. Brubaker, and J. Steele, "Results from the coded aperture neutron imaging system," in *IEEE Nuclear Science Symposuim & Medical Imaging Conference*, 2010, pp. 1640–1646
[10] P. Hausladen, J. Newby, F. Liang, and M. Blackston, "The Deployable Fast-Neutron Coded- Aperture Imager : Demonstration of Locating One or More Sources in Three Dimensions Prepared by," 2013
[11] N. Mascarenhas, J. Brennan, K. Krenz, P. Marleau, and S. Mrowka, "Results with the neutron scatter camera," in *2008 IEEE Nuclear Science Symposium Conference Record*, 2008, vol. 56, no. 3, pp. 3368–3371.
[12] J. Brennan, E. Brubaker, R. Cooper, M. Gerling, C. Greenberg, P. Marleau, N. Mascarenhas, and S. Mrowka, "Measurement of the Fast Neutron Energy Spectrum of an (241)Am-Be Source Using a Neutron Scatter Camera," *IEEE Trans. Nucl. Sci.*, vol. 58, no. 5, pp. 2426–2430, Oct. 2011
[13] A. Poitrasson-Rivière, M. C. Hamel, J. K. Polack, K. L. Mcmillan, K. Ide, S. D. Clarke, M. Flaska, and S. A. Pozzi, "Design Considerations of a Dual-Particle Imager for Non-Proliferation Applications," in *Proceedings of INMM 52nd Annual Meeting*, 2011
[14] J. Brennan, E. Brubaker, A. Nowack, J. Steele, M. Sweany, and D. Throckmorton, "Bubble masks for time-encoded imaging of fast neutrons," in *2013 IEEE Nuclear Science Symposium and Medical Imaging Conference (2013 NSS/MIC)*, 2013, pp. 1–7.
[15] J. Brennan, E. Brubaker, M. Gerling, N. Le Galloudec, P. Marleau, K. McMillan, and A. Nowack, "Results from field tests of the two-dimensional Time-Encoded Imaging System," 2014
[16] J. Goldsmith, J. Brennan, M. Gerling, S. Kiff, N. Mascarenhas, and J. Van de Vreugde, "MINER - A Mobile Imager of Neutrons for Emergency Responders," in *Sandia National Laboratories Internal Report*, 2014
.

imaging systems requires the development of robust reconstruction and analysis algorithms capable of detecting, localizing, and characterizing any radioactive materials that might be present.

DETAILED DESCRIPTION OF EXPERIMENT/METHOD:

The bulk of the effort in this project has been focused on advancing the maximum-likelihood expectation-maximization (MLEM) algorithm from pure image reconstruction to simultaneous reconstruction of both the image and emitted energy spectra with statistical an systematic uncertainty estimation. This required moving from a system response matrix based off of a specific source (namely Cf^{252}) to a generalized, source-independent matrix. The use of such a matrix allows for an emitted spectrum to be reconstructed for every source pixel. Experimental validation of algorithms and uncertainty estimation was accomplished with the University of Michigan Dual-Particle Imaging system (DPI).

The Dual-Particle Imager

The DPI is a radiation detection system capable of imaging photons and fast neutrons. The DPI was designed for localization and energy spectroscopy for both particle types. These capabilities make the DPI a powerful measurement tool for applications that necessitate the detection, localization, and characterization of SNM.

The DPI combines the concepts of a Compton camera and a neutron-scatter camera into a single device. The Compton camera is a mature concept for photon imaging that has been used for many years in fields such as medical imaging and astronomy. Neutron-scatter cameras are the fast-neutron analog to Compton cameras. Recently, Compton cameras and neutron-scatter cameras have been developed for non-proliferation and safeguards applications[20].

Compton cameras and neutron-scatter cameras fall into a subset of imaging devices known as scatter cameras. Scatter cameras leverage the mechanics of particle elastic scattering to determine the incident energy and direction of a detected particle. To make these determinations,

---

[17] A. C. Madden, P. F. Bloser, D. Fourguette, L. Larocque, J. S. Legere, M. Lewis, M. L. McConnell, M. Rousseau, and J. M. Ryan, "An imaging neutron/gamma-ray spectrometer," in *Proceedings of SPIE 8710, Chemical, Biological, Radiological, Nuclear, and Explosives (CBRNE) Sensing*, 2013, vol. 8710, p. 87101L

[18] A. Poitrasson-Rivière, M. C. Hamel, J. K. Polack, M. Flaska, S. D. Clarke, and S. A. Pozzi, "Dual-particle imaging system based on simultaneous detection of photon and neutron collision events," *Nucl. Instruments Methods Phys. Res. Sect. A Accel. Spectrometers, Detect. Assoc. Equip.*, vol. 760, pp. 40–45, Oct. 2014

[19] S. T. Brown, Y. A. Boucher, J. Mann, Y. Zhu, and Z. He, "Thermal neutron source location using a 3-D position-sensitive CdZnTe detector array," in *2013 IEEE Nuclear Science Symposium and Medical Imaging Conference (2013 NSS/MIC)*, 2013, pp. 1–5

[20] Y. F. Du, Z. He, G. F. Knoll, D. K. Wehe, and W. Li, "Evaluation of a Compton scattering camera using 3-D position sensitive CdZnTe detectors," *Nucl. Instruments Methods Phys. Res. Sect. A Accel. Spectrometers, Detect. Assoc. Equip.*, vol. 457, no. 1–2, pp. 203–211, Jan. 2001.

.

scatter cameras require that an incident particle undergo a minimum of two interactions within the system, including at least one elastic scatter.

The DPI uses a two-plane geometry, similar to the one depicted in Figure 1, in which each plane is comprised of a 4×4 array of scintillators[21]. The front plane uses EJ-309 organic liquid scintillators as a scattering medium for both neutrons and photons. The back plane uses EJ-309 organic liquid scintillators as a neutron scattering medium, and NaI(Tl) scintillators, as a photon absorption medium.

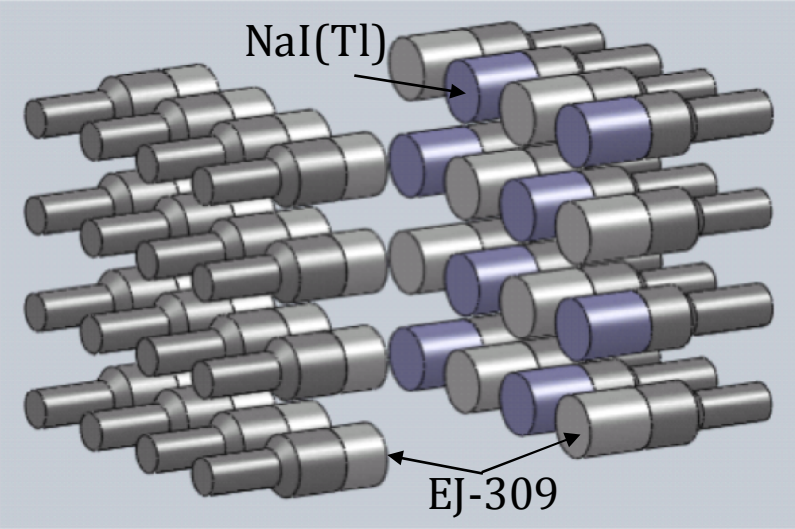

Figure 1. Schematic of the DPI geometry. Silver detectors represent EJ-309 organic liquid scintillators while blue detectors represent NaI(Tl) scintillators.

The two detector types in the second plane are arranged in a checkerboard pattern as seen in Figure 1. All detectors are oriented such that the photomultiplier tubes face outward from the center of the system, which reduces the probability of scatters occurring between an interaction in the front plane and an interaction in the back plane. While the DPI is 4-π sensitive, the best results are achieved when the system is oriented such that the front plane is between the radioactive material (source) and the back plane[22]. In practice, if a source is detected behind the system, the system should be rotated such that the front plane points towards the source.

The system response matrix is computed using MCNPX-PoliMi. Neutrons and photons are simulated separately due to the different number of simulated particles required to achieve a reasonable level of statistics. Spatially, the source was uniformly distributed as a 2π hemisphere located in front of the system. The radius of this hemisphere was chosen to be 2 m, which is a

[21] M. C. Hamel, A. Poitrasson-Rivière, J. K. Polack, S. D. Clarke, M. Flaska, and S. A. Pozzi, "Design and Analysis of a Two-Plane Dual-Particle Imaging System," in *Proceedings of the INMM 54th Annual Meeting*, 2013
[22] A. Poitrasson-Rivière, "Development of a Dual-Particle Imaging System for Nonproliferation Applications," 2016
.

typical source-to-detector distance used in experiments. However, very little uncertainty is introduced when reconstructing a source located at a different radius.

The continuous hemispherical distribution allows for the image-pixel bin sizes to be determined at will during the binning process. If the image pixels are binned uniformly in degrees along the azimuthal and inclination direction, then pixels near the image poles (ϕ={0,180}) will have smaller area (and therefore fewer emitted counts) than those towards the equator (ϕ=90). This trend is shown in Figure 2 (a), which displays the number of particles emitted from each bin for 5°×5° image pixels.

The distribution shown in Figure 2 (a) is somewhat advantageous because most experiments are performed with the source close to ϕ=90°, which makes it desirable to have lower relative uncertainty in this region. While sources will not always be well aligned with the DPI in field use, we have demonstrated that the DPI will still be able to detect and accurately characterize sources at off-center inclinations (and azimuths). If higher statistical fidelity is required, then a field-deployable DPI could be rotated to better position the source within the FOV.

Alternatively, a new simulation technique could be developed to account for this statistical bias at the expense of increased simulation time.

The area of a pixel centered at an arbitrary inclination ϕ relative to a pixel centered at an inclination of 90° is distributed as cos(ϕ-90°), as shown in Figure 2 (b). If during the binning process pixels near the poles are found to have undesirably low statistics, then those pixels can be ignored by reducing the FOV. The relative area of each pixel is accounted for when determining M_s for each s.

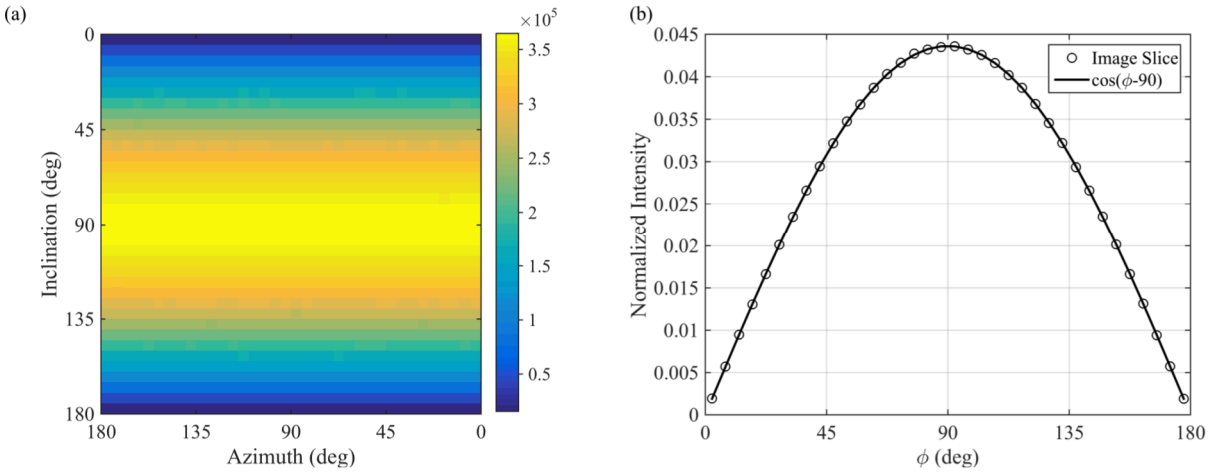

Figure 2. Image of the number of particles emitted from each 5°×5° pixel for a hemispherically distributed source with 3×10^8 total emissions (a). Number of emissions from each pixel in a vertical slice of (a) plotted with the shifted cosine function that determines this distribution (b). Both curves in (b) are normalized by their integral.

.

To improve simulation efficiency, the direction of the emitted particle was sampled from a cone with an axis drawn between the randomly sampled emission position and the geometric center of the DPI. The opening angle of the cone was defined such that the cone would be tangent to a sphere fully encompassing the DPI, as shown in Figure 3. The system sphere radius is 76.5 cm and so for a fixed source hemisphere radius of 200 cm, the opening angle is 22.5°. This angle corresponds to a solid angle of 0.48 steradians, which is ~3.8% of a fully isotropic source. The result of this conical sampling is that each $a_{d,s}$ is the probability of measuring a particle emitted towards the DPI from source bin s in observation bin d. Therefore, the solution yields an estimate of the number of particles emitted by source distribution $\boldsymbol{x}$ toward the system.

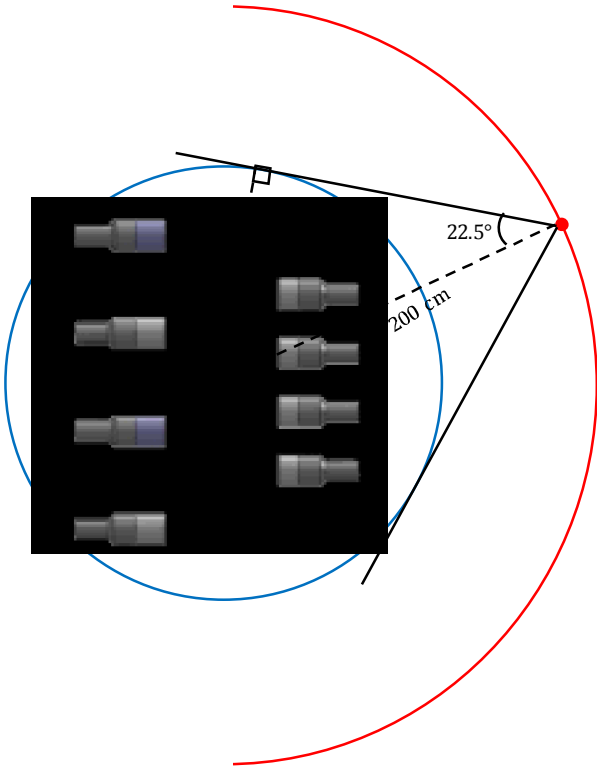

Figure 3. Schematic of system matrix simulation technique. The red curve represents the hemisphere of possible source locations and the blue circle represents the sphere encompassing the DPI. Particles are emitted from a conical distribution tangent to the system sphere. Schematic is not to scale.

MCNPX does not provide the capability to define the emission direction as function of a continuously sampled source space. This functionality was added through a patch to the MCNPX-PoliMi source code[23]. The simulation was set up such that, regardless of the starting position, particle direction was sampled from a cone aligned with the positive the z-axis. The patch computes the rotation matrix required to rotate between the positive z-axis and the desired cone axis, which points between the

[23] A special thank you is owed to Matthew Marcath for his assistance in the development of this patch.

.

starting position of the particle and center of the DPI. This matrix rotates the original sampled direction such that the particle is emitted towards the DPI.

System Matrix Uncertainty

Uncertainty in the system matrix is a function of both the number of particles simulated during computation and the size of the bins chosen. The level of statistical uncertainty present in the system matrix is assessed based on the relative error of the sensitivity map. The sensitivity map is defined as the column-wise sum of the system matrix and, in this work, defines the total probability of the DPI detecting a particle emitted toward the system from each source-space bin, *s*. Uncertainty in each sensitivity bin is defined as the square root of the number of counts detected in each sensitivity bin. While the sensitivity term for each *s* accounts for the number of particles emitted from *s*, the sensitivity uncertainty term is only dependent on the number of counts detected.

During the simulation process, uncertainty in the sensitivity bins was tracked by successively populating new system matrices with increasing numbers of total counts. Figure 4 plots, as a function of seeds simulated, the fraction of sensitivity bins that have obtained 10%, 5%, and 2.5% relative uncertainty. This plot shows that almost 100% of sensitivity bins have achieved better than 10% relative uncertainty for both particle types. For neutrons, greater than 99% of sensitivity bins have better than 5% uncertainty and over 80% have better than 2.5% uncertainty. For photons, greater than 90% of sensitivity bins have better than 5% uncertainty and over 35% of sensitivity bins have better than 2.5% uncertainty. For a given number of seeds, the photon system matrix has a lower number of statistically significant sensitivity bins than the neutron system matrix because the photon system matrix has four times more source-space bins. As a result, more photon seeds were simulated in an attempt to achieve similar levels of overall uncertainty.

.

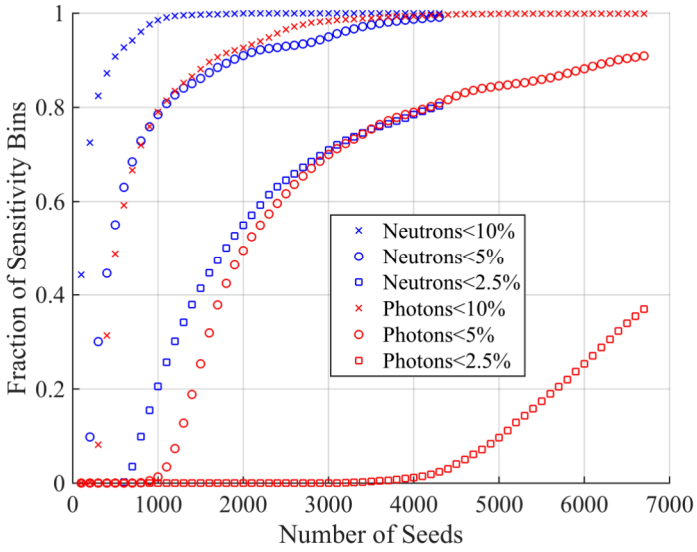

Figure 4. Fraction of sensitivity bins that have achieved a 10%, 5%, and 2.5% relative uncertainty. Neutrons are shown in blue and photons are shown in red. Each step along the x-axis represents a system matrix populated using the events for that number of seeds.

While Figure 4 gives a reasonable understanding of the system matrix as a whole, it is also useful to know how the uncertainty varies in source space. This information is available through the sensitivity images and their associated error maps. The sensitivity image for a particular energy bin shows the efficiency as a function of emission location (i.e. the number of particles detected divided by the number of particles emitted). Higher intensity in the sensitivity map indicates source locations that will be more efficiently measured by the DPI. The error map for a particular energy bin shows the relative error associated with each location, which is found by dividing the Poisson uncertainty by the number of particles detected. The shape of a sensitivity image and its associated error map will be similar (but inverted); however, the error maps will be impacted by the $\cos(\phi\text{-}90°)$ trend because they are dependent only on the number of particles detected and not the number of particles emitted. When viewing these images, note that the color bars are allowed to vary with energy so that the shapes of each image is apparent.

Figure 5 shows the neutron sensitivity images and the associated uncertainty maps for the source-space energy bins ranging between 2.0 and 2.4 MeV (a, b), between 4.8 and 5.2 MeV (c, d), and between 8.0 and 8.4 MeV (e, f). The shape of the sensitivity images is similar at all three energies, which is expected because the scattering angle probability distribution for a neutron elastic scattering on ^{1}H is not dependent on energy. The maximum efficiency decreases as a function of energy: dropping from ~0.022% to ~0.013% between 2 and 8 MeV.
The highest sensitivity is found ~20° from the center of the FOV with a slight drop toward the center. This drop in sensitivity is a result of the system geometry, which dictates a lower scatter angle between detector pairs for neutrons incident from the center of the FOV. Low-angle scatters deposit a lower fraction of incident energy, and are therefore are more likely to fall below threshold in the front plane. A drop in sensitivity is also seen towards the edges of the

.

FOV, which corresponds to locations that predominantly require large scatter angles for a neutron to travel toward a back plane detector. As a result, these neutrons are less likely to have enough energy to interact above threshold in the back plane.

The uncertainty maps show that the lowest uncertainty is towards the center of the FOV and that a relative error below 2.5% has been achieved at all energies for a large portion of the FOV, with higher uncertainties appearing towards the edges (especially the poles). The uncertainty maps also show that there are similar levels of uncertainty at all energy ranges, which is a result of the weighting applied to the simulated energy spectrum.

.

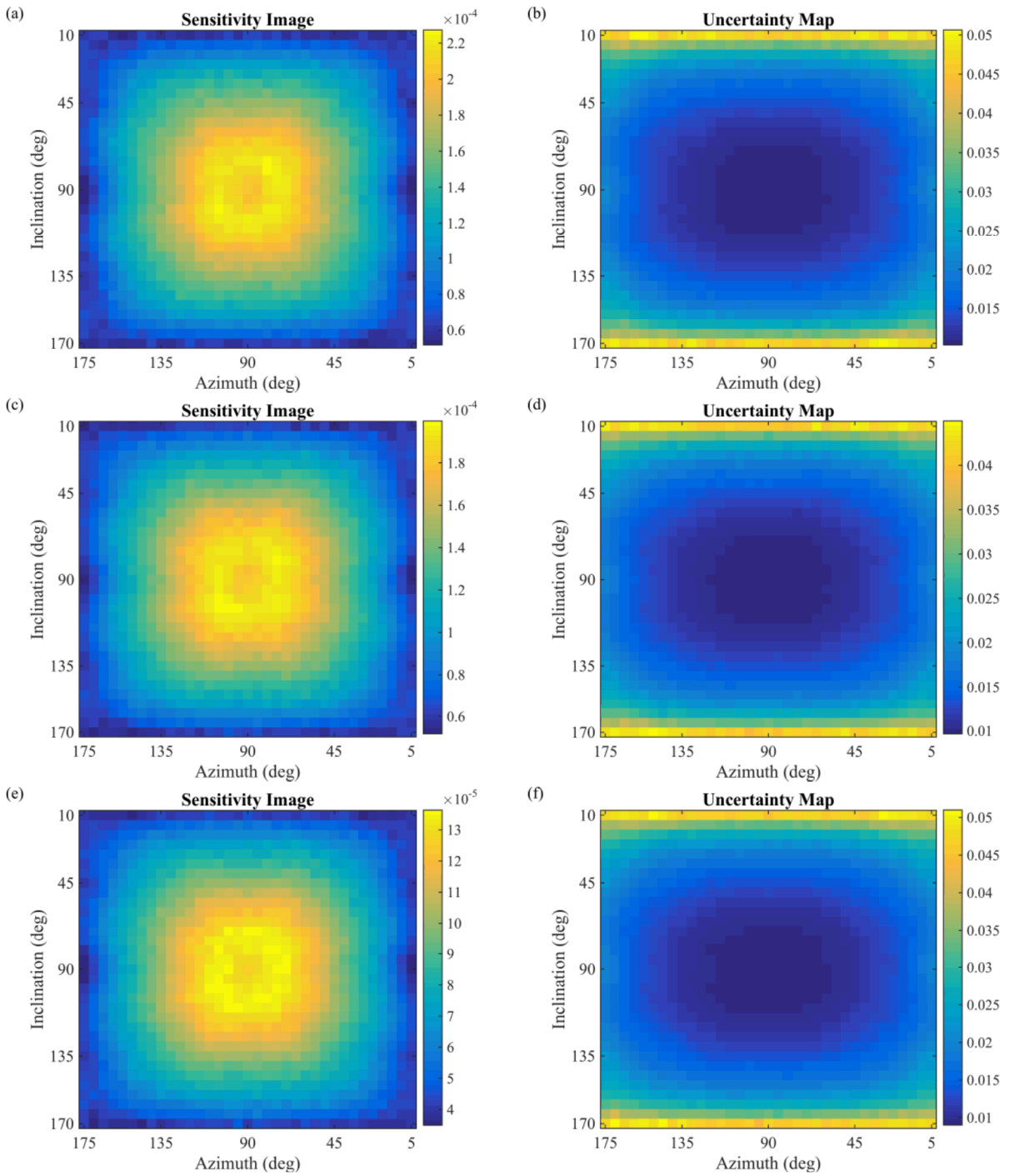

Figure 5. Neutron sensitivity images and the associated statistical uncertainty maps for the source-space energy bins ranging between 2.0 and 2.4 MeV (a, b), between 4.8 and 5.2 MeV (c, d), and between 8.0 and 8.4 MeV (e, f). The color scale for the sensitivity images represent detection efficiency while the color scale for the uncertainty maps represent the relative Poisson error.

.

Figure 6 shows the photon sensitivity images and the associated uncertainty maps for the source-space energy bins ranging between 300 and 350 keV (a, b), between 650 and 700 keV (c, d), and between 1300 and 1350 keV (e, f). Similar to the neutron sensitivity maps, the photon sensitivity maps show a drop in sensitivity towards the center and edges of the FOV, which is due to the system geometry. Unlike neutrons, the shape of the sensitivity images changes as a function of energy. This variation is because the scattering angle probability distribution for Compton scattering changes as a function of energy as determined by the Klein-Nishina formula. Higher energy photons have a more forward-directed scatter probability, and therefore, the sensitivity image for higher energy photons is also more forward directed. Similar to the neutron uncertainty maps, the photon uncertainty maps show that the highest areas of uncertainty are towards the edge of the FOV. Again, the range of uncertainty is relatively constant at all energy ranges as a result of the energy spectrum weighting.

It is important to remember that the uncertainty in each sensitivity bin is a function of the bin sizes chosen. That is, for the same set of system matrix data, the uncertainty in each sensitivity bin can be reduced by simply moving to coarser binning. For example, doubling the size of the energy bins used will result in half as many source-space bins and will improve uncertainty in each sensitivity bin by a factor of approximately $\sqrt{2}$. The reduction in uncertainty would of course be accompanied by a loss of precision.

.

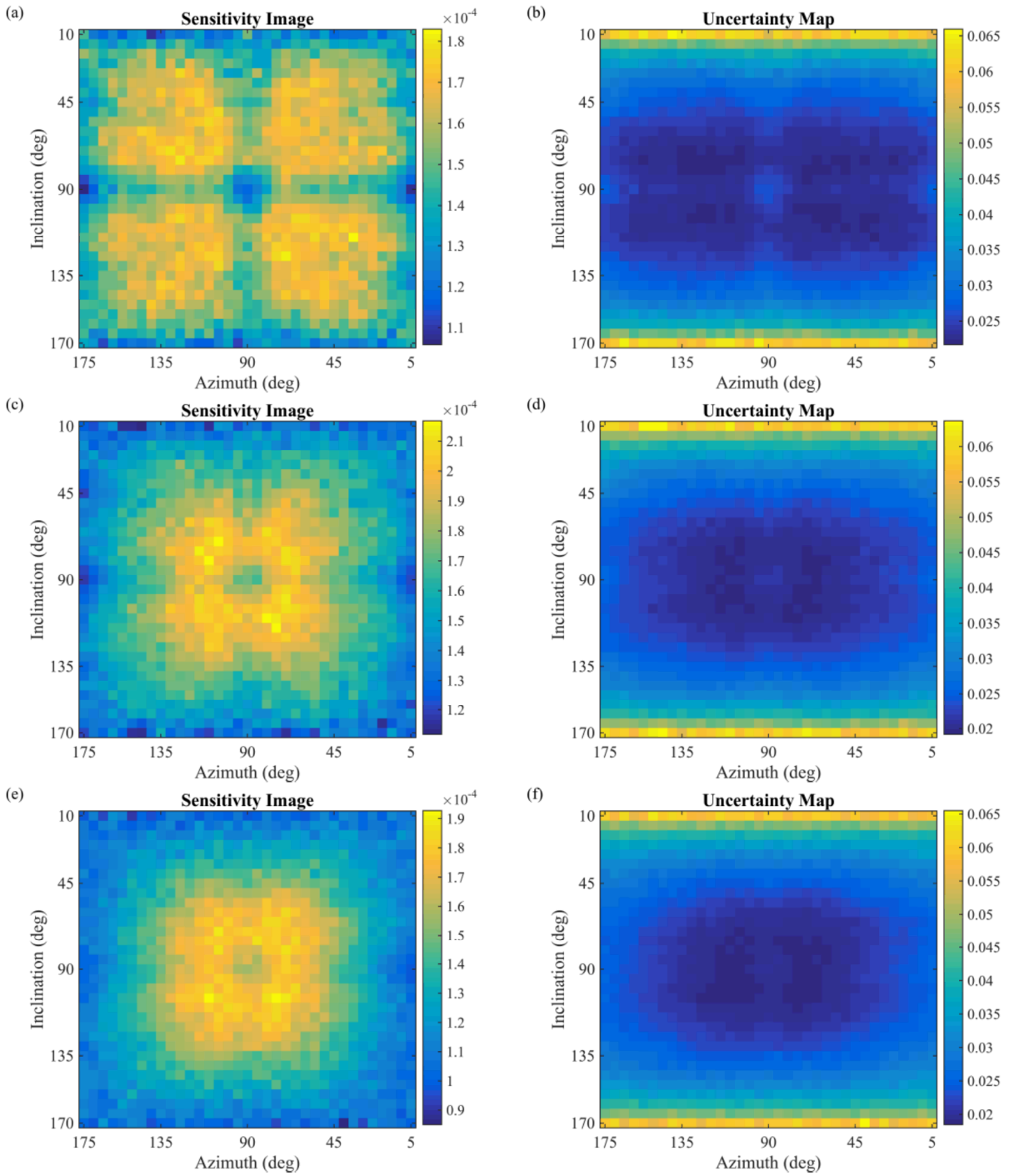

Figure 6. Photon sensitivity images and the associated statistical uncertainty maps for the source-space energy bins ranging between 300 and 350 keV (a, b), between 650 and 700 keV (c, d), and between 1300 and 1350 keV (e, f). The color scale for the sensitivity images represent detection efficiency while the color scale for the uncertainty maps represent the relative Poisson error.

.

Sparsity

It is important to note that not all observation bins in a specific source bin have non-zero probability due to physical constraints. However, the specific location of the zero-probability observation bins will change from source bin to source bin. For example, it may *not* be possible for a particle from location s_1 to be detected in bin $a_{d,1}$ while it *is* possible for a particle from location s_2 to be detected in in bin $a_{d,2}$. With extensive enough binning, only a small fraction of the system matrix elements will be non-zero, resulting in a sparse matrix.

MATLAB has a built-in sparse matrix framework based on the compressed-sparse-column format[24]. This technique reduces the data being stored to only the non-zero elements and their respective indices. Computation time is also reduced by ignoring unnecessary operations involving zero-valued elements.

The use of sparse matrices makes the relatively small binning sizes used in this work possible. Storing full response matrices of these sizes in double precision would require ~40 GB and ~1 TB for neutrons and photons, respectively. However, taking advantage of sparsity reduces the memory requirements to less ~1.6 GB for neutrons and ~6.0 GB for photons.

Gamma-Ray Experiment

To demonstrate the performance of the spectral isolation technique that we have developed at localizing gamma-ray peaks, a 15-minute measurement was made of an 87.4-μCi ^{137}Cs source and an 88.6-μCi ^{22}Na source. Both sources were at a 2-m standoff with the ^{137}Cs located at (60°, 90°) and the ^{22}Na located at (120°, 90°). A total of 8.97×10^4 photon events were recorded. A photograph of the experimental setup is shown in Figure 7.

[24] MathWorks, "Copmutational Advantages of Sparse Matrices." [Online]. Available: http://www.mathworks.com/help/matlab/math/computational-advantages-of-sparse-matrices.html .

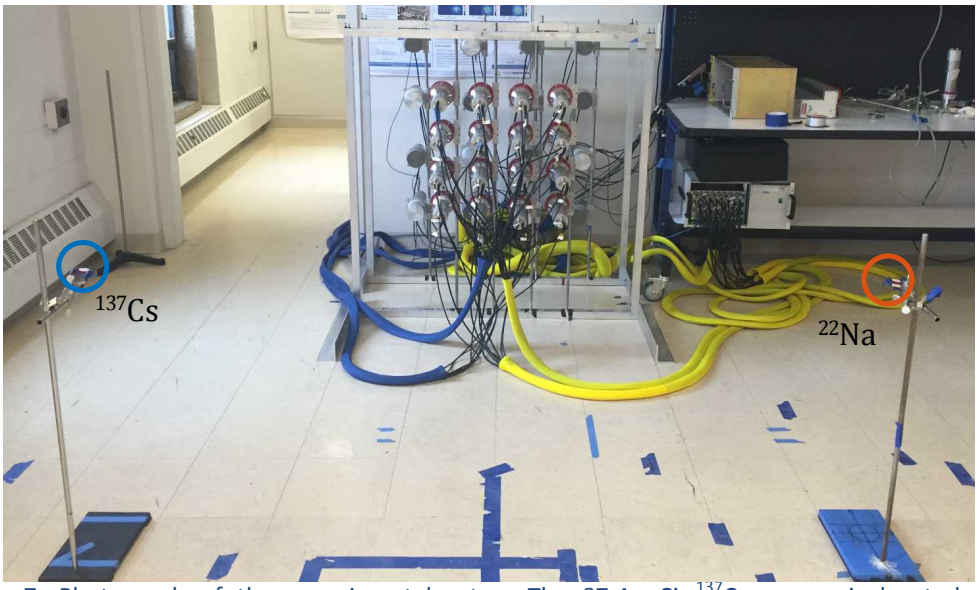

Figure 7. Photograph of the experimental setup. The 87.4 µCi ^{137}Cs source is located at (2 m, 60°, 90°) and the 88.6-µCi ^{22}Na source is located at (2 m, 120°, 90°).

Table 1 lists the intensities of the gamma rays emitted by these sources as well as the expected number of gamma rays emitted toward the DPI during a 15-minute measurement (i.e. the amount that would be expected in a perfectly unfolded spectrum). The 0.511 MeV gammas are not emitted directly by ^{22}Na, but are instead caused by positron annihilation resulting from a β^+ decay of ^{22}Na.

Table 1. Intensity of gamma-ray emissions from ^{137}Cs and ^{22}Na and the expected number of unfolded counts from a 15-minute measurement using a 2-m standoff.

Source	Energy (MeV)	Intensity	Expected Counts
^{137}Cs	0.662	0.851	9.41×10^{7}
^{22}Na	0.511	1.808	2.02×10^{8}
^{22}Na	1.274	0.999	1.12×10^{8}

Figure 8 shows the reconstructed image as well as the isolated photon spectra for the two 5×5 Regions of Interest (ROIs) outlined on the image. The two hotspots are both centered at the correct locations. The isolated spectra are also well aligned with the expected energies. The ROI centered at (60°, 90°) shows a peak in the energy bins ranging between 0.6 and 0.7 MeV, encompassing the 0.662 MeV emission from ^{137}Cs. The ROI centered at (120°, 90°) shows one peak in the energy bins ranging between 0.45 and 0.55 MeV and one peak in the energy bins ranging between 1.2 and 1.3 MeV, which encompass the 0.511 MeV and 1.274 MeV peaks from ^{22}Na, respectively.

.

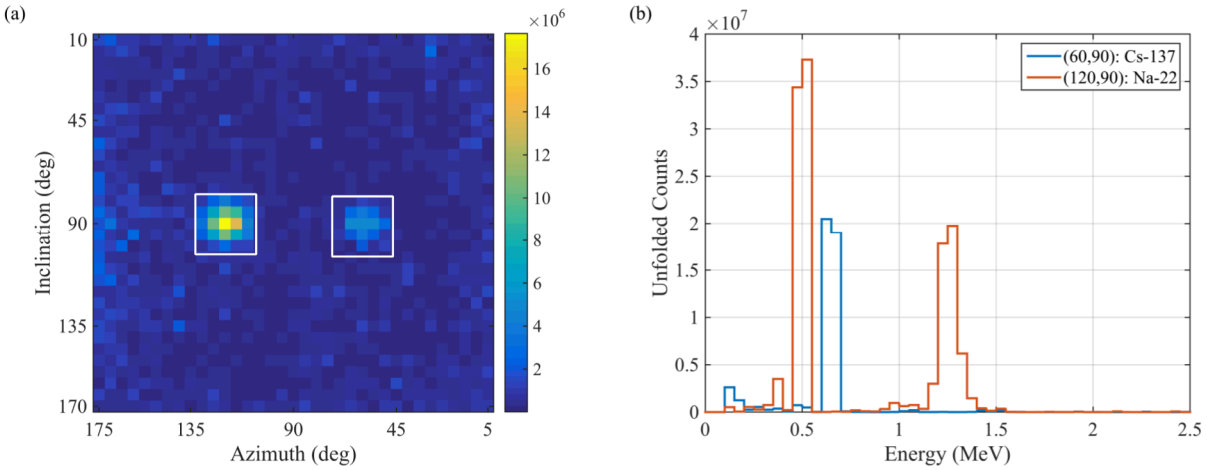

Figure 8. Reconstructed image (a) and isolated spectra (b) for a 15-minute measurement of .an 87.4 µCi ^{137}Cs source located at (2m, 60°, 90°) and an 88.6-µCi ^{22}Na source located at (2m, 120°, 90°). White boxes in the image denote the 5×5 pixel ROIs used to generate the isolated spectra.

Improvement Over Basic Reconstruction Techniques

For comparison, Figure 9 shows the simple-backprojection image and coincidence spectrum for the same data. It is clear that the MLEM-based reconstruction technique has improved the visibility of the ^{137}Cs hotspot in the image. Additionally, the unfolded spectra provide a more accurate representation of the emitted distributions than the coincidence spectrum, which includes background events and significant contributions from the Compton continuum of each photopeak.

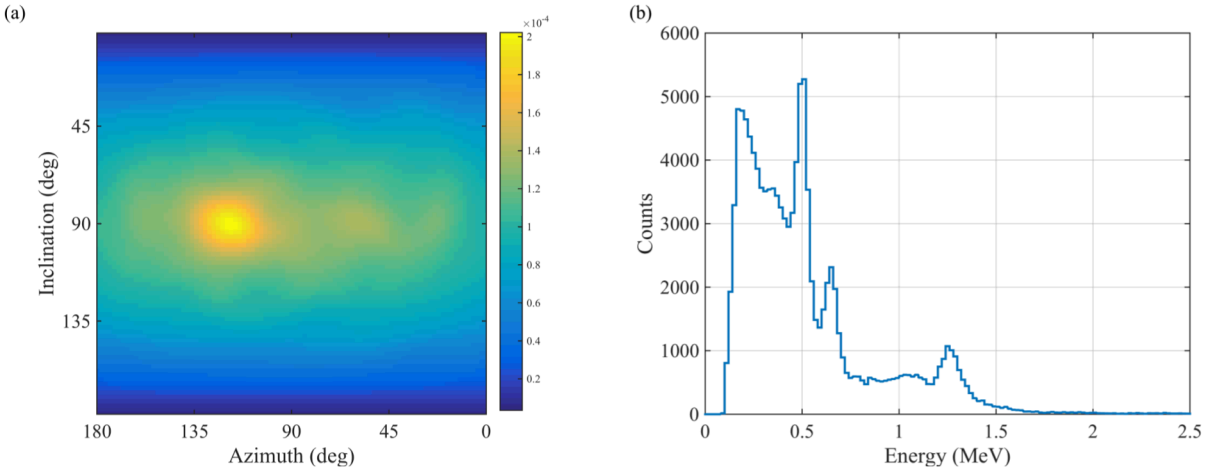

Figure 9. Simple backprojection image (a) and coincidence spectrum (b) for a 15-minute measurement of .an 87.4 µCi ^{137}Cs source located at (2 m, 60°, 90°) and an 88.6-µCi ^{22}Na source located at (2 m, 120°, 90°).

Image Energy Windowing

In Figure 9(a), the ^{137}Cs hotspot has a lower intensity than the ^{22}Na hotspot, which is expected due to the relative number of gamma emissions between the two sources. It is possible to

.

improve the contrast of the ^{137}Cs hotspot by restricting the energy range of the image. Figure 10(b), which shows the image for the 0.6-0.7 MeV energy range, demonstrates this effect. In addition to improving the contrast of the ^{137}Cs hotspot, the use of an energy window has removed the ^{22}Na hotspot from the image, and has also reduced the image noise. A similar technique can also be used on the ^{22}Na hotspot, which is demonstrated in Figure 10 (c) and (d) for the 0.45-0.55 MeV range and the 1.15-1.35 MeV range, respectively. In all three images, only the expected hotspot is shown, which is encouraging considering the proximity of the 0.511 MeV and 0.662 MeV lines (relative to the energy resolution of the system). Additionally, the improved contrast of the ^{137}Cs hotspot provided by the windowed image demonstrates the utility of the spectrum-isolation technique for analyzing environments containing multiple sources of different intensities.

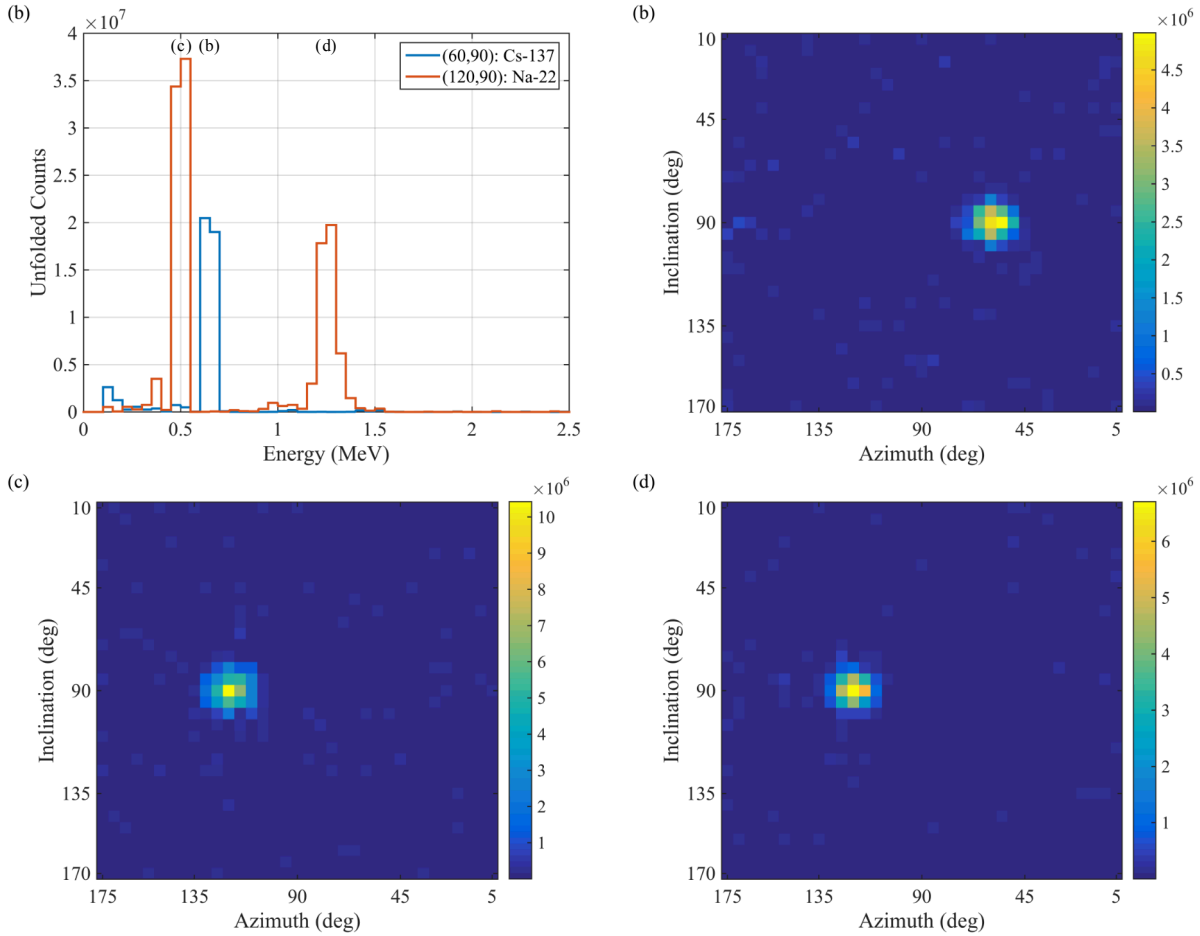

Figure 10. Images reconstructed over various energy ranges of the isolated spectra shown in (a). ^{137}Cs hotspot is shown using the 0.60-0.70 MeV energy range (b). ^{22}Na hotspot is shown using two different energy ranges: 0.45-0.55 MeV (c) and 1.15-1.35 MeV (d).

.

Statistical Uncertainty

As with any radiation measurement, the data collected by the DPI is subject to the statistical deviations associated with a Poisson process. That is, two measurements of the same source distribution will yield different measured data. If the measurement time is long enough, then the underlying distributions will prevail and multiple realizations will converge to the same result within the limits of their associated statistical uncertainty. In the typical Poisson counting process, the standard deviation of a measured quantity can be calculated as the square root of the number of measured events. This straightforward technique can be directly applied, for example, to the coincidence spectra reconstructed by the DPI. However, the unfolded counts calculated by the spectrum-isolation technique are a result of propagating a measured distribution through a non-linear process (namely MLEM)[25]. While it is certainly important to quantify the uncertainty in ML solutions, the propagation of statistical uncertainty through the MLEM algorithm is not straightforward.

As with any measurement, the variance in the solution can be estimated by performing multiple, repetitive measurements of the same distribution. However, in many non-proliferation and safeguards applications it is unfeasible, or sometimes impossible, to perform multiple measurements. The need to perform multiple measurements could be alleviated by dividing the measured data set into several smaller subsets; however, this comes at the cost of higher statistical fluctuations due to the reduced number of events in each data subset. The bootstrap technique, described in the next section, facilitates estimation of statistical uncertainty without the need to perform multiple measurements or subdivide the measured data.

Bootstrapping

The bootstrap is a statistical technique used for estimating the variance in a measurement when it is impractical to perform multiple repetitive measurements[26]. The technique has been used with success in several medical imaging studies related to positron-emission tomography. The bootstrap works by resampling (with replacement) the measured data set to produce K-1 bootstrap data realizations. Each of the bootstrap realizations, as well as the measured realization, can then be processed with MLEM resulting in K bootstrap solutions from which the variance can be estimated. It is worth noting that generating K bootstrap solutions will increase the computation time by approximately a factor of K. However, this additional cost could be easily reduced by processing each realization in parallel across several cores.

In this work, the bootstrap data realizations are generated from the list-mode data used to fill the binned data vector $\boldsymbol{b}$. As a reminder, the list mode data contains the information required to sort each event into bins, namely the reconstructed energy, reconstructed angle, and detector pair. If a data set contains N measured events, then each bootstrap data set will also contain N total events. While the measured list mode data will include one entry for each individual measured event, the

[25] H. H. Barrett, D. W. Wilson, and B. M. W. Tsui, "Noise properties of the EM algorithm. I. Theory," *Phys. Med. Biol.*, vol. 39, no. 5, pp. 833–846, May 1994

[26] B. Efron and R. J. Tibshirani, "An Introduction to the Bootstrap," *SIAM Rev.*, vol. 36, no. 4, pp. 677–678, Dec. 1994

.

bootstrap realizations may include zero, one, or many entries for each event. This approach is similar to the non-parametric list-mode technique proposed by Dahlbom[27] and tested by Lartizien et al.[28] and (with some modifications) Ibaraki et al.[29].

The variation in the bootstrap data-sets will result in variation across the bootstrap solutions, which can be used to estimate the statistical properties of the measured data set. For example, the variance, σ^2, of a region of interest, R, can be calculated as:

Equation 1

$$\sigma^2 \equiv \mathrm{var}(R) = \frac{1}{K-1}\sum_{k=1}^{K}(R_k - \mu)^2 \quad ,$$

where R_k is the number of counts in R for the k^{th} bootstrap solution and μ is the mean counts in R across all realizations:

Equation 2

$$\mu = \frac{1}{K}\sum_{k=1}^{K} R_k$$

Haynor and Woods established that for an image, R can include any number of contiguous or disjoint pixels[30]. This idea can be extended to the spectrum-isolation technique by defining R to be an individual energy bin of the isolated spectra. In this way, the uncertainty of each energy bin in the isolated spectrum can be estimated regardless of the size or shape of the ROI used to generate the spectrum.

Validation of Bootstrapping

Prior to relying on the bootstrap technique to estimate solution variance, it is important to validate that the error predicted through bootstrapping is representative of the error across repetitive measurements. A series of 50 5-minute measurements were performed with a 4.4-mCi ^{252}Cf source located at (2 m, 90°, 90°). These measurements resulted in an average of 22,221 neutron counts and 206,939 photon events per 5-minute segment.

---

[27] M. Ibaraki, K. Matsubara, K. Nakamura, H. Yamaguchi, and T. Kinoshita, "Bootstrap methods for estimating PET image noise: experimental validation and an application to evaluation of image reconstruction algorithms," *Ann. Nucl. Med.*, vol. 28, no. 2, pp. 172–182, Feb. 2014

[28] C. Lartizien, J.-B. Aubin, and I. Buvat, "Comparison of Bootstrap Resampling Methods for 3-D PET Imaging," *IEEE Trans. Med. Imaging*, vol. 29, no. 7, pp. 1442–1454, Jul. 2010.

[29] M. Ibaraki, K. Matsubara, K. Nakamura, H. Yamaguchi, and T. Kinoshita, "Bootstrap methods for estimating PET image noise: experimental validation and an application to evaluation of image reconstruction algorithms," *Ann. Nucl. Med.*, vol. 28, no. 2, pp. 172–182, Feb. 2014

[30] D. R. Haynor and S. D. Woods, "Resampling estimates of precision in emission tomography," *IEEE Trans. Med. Imaging*, vol. 8, no. 4, pp. 337–343, 1989.

.

Equation 1 and Equation 2 are also used to assess the mean and variance across measured data sets. However, for measured data sets, k now represents a solution from a unique measurement rather than a bootstrapped realization.

The statistical properties estimated using 50 bootstrapped realizations of a single 5-minute measurement were compared to the statistical properties computed directly from the full set of 50 repeated measurements. Comparisons were made for isolated spectra, full images, and gross counts within an image ROI. It was shown that bootstrapping provides a reasonable estimate of the relative uncertainty, defined as σ/μ, in a solution. However, while the measured estimate of μ increases in accuracy with the number of independent measurements, the bootstrapped estimate of μ does not vary significantly from the μ of the original data. An improved estimate in μ is not obtained via bootstrapping because the bootstrapped realizations are still subject to the statistical fluctuations of the single data set from which they were generated. These fluctuations are averaged out when multiple independent measurements are performed. These findings are consistent with conclusions drawn by Lartizien et al.[28], and Ibaraki et al.[29].

Systematic Uncertainties

The bootstrapping technique provides a reasonable method for estimating the statistical uncertainty in a spectrum-isolation solution. However, it is also important to understand how systematic uncertainties within the system matrix impact the shape of the isolated spectra. Chapter 4 demonstrated that it is possible to obtain reasonably accurate energy spectra from the region around a detected source, even when the source was not located at the 2-m standoff used in the system matrix. Ideally, measurements of the same source will yield the same results, regardless of the location or standoff distance of the source. However, as the position of the source changes, the measured distribution recorded in the data vector, $\boldsymbol{b}$, will also change. These distributions are propagated through the system matrix during reconstruction and therefore any spatially dependent bias within the system matrix could cause the final solutions to be different. It is possible to estimate the extent of these systematic uncertainties by measuring the same source at different locations and evaluating any changes in the solution.

This study was focused on how systematic uncertainties impact the shape of the isolated energy spectra, which are of particular importance because they are used to characterize the nature of the detected radioactive material. If the shape of the energy spectra varies greatly with source location, characterization becomes much more difficult. However, if the shapes are similar then it is possible to reliably analyze isolated spectra through techniques such as template matching (i.e. comparing a measured spectrum to a known reference spectrum).

Testing for Systematic Uncertainty

To test how systematic uncertainties within the system matrix vary, a series of N measurements were performed, each with the source at a different location (or standoff). The spectrum-isolation solution was then computed for each measurement and the isolated spectrum is generated from the 5×5-pixel region centered at the source location. The bootstrap technique was used to

.

estimate the mean, μ_n, and standard deviation, σ_n, for each measured spectrum. These estimates are made for each energy bin; the following analysis was performed on a bin-by-bin basis.

The observed mean, μ_T, and variance, σ_T^2, across the N measurements are computed using Equation 3 and Equation 4,

Equation 3

$$\mu_T = \frac{1}{N}\sum_{n=1}^{N}\mu_n$$

Equation 4

$$\sigma_T^2 = \frac{1}{N-1}\sum_{n=1}^{N}(\mu_n - \mu_T)^2$$

where the total observed uncertainty, σ_T, will be equal to the quadrature sum of the statistical uncertainty, σ_S, and the systematic uncertainty, σ_Q:

Equation 5

$$\sigma_T^2 = \sigma_S^2 + \sigma_Q^2$$

If, σ_S^2 is known, then a chi-squared test can be used to check if σ_T^2 is larger than what is expected due to statistical fluctuations alone by testing the null hypothesis $\sigma_T^2 \leq \sigma_S^2$:[31]

Equation 6

$$\chi^2 = \frac{(N-1)\sigma_T^2}{\sigma_S^2}$$

If the null hypothesis is rejected, then a systematic uncertainty has been observed. However, if the null hypothesis is accepted, then no systematic uncertainty has been observed. Accepting the null hypothesis does not necessarily imply that there is no systematic uncertainty present, only that it is not large enough (relative to the statistical uncertainty) to be observed.

While an exact model for σ_S^2 is not known, it can be approximated by propagating each of the bootstrapped statistical uncertainties, σ_n, through the calculation of μ_T such that

[31] A. O. Hero, *Statistical Methods for Signal Processing*. XanEdu, 2013

.

Equation 7

$$\sigma_S^2 \cong \frac{1}{N}\sum_{n=1}^{N}\sigma_n^2$$

This test may be limited by the accuracy of the bootstrap estimate of the statistical uncertainty and also by the number of measurements available for computing μ_T and σ_T. However, it should provide a reasonable estimate as to whether any significant systematic deviations are present.

Impact of Location within Field of View

To test how systematic uncertainties within the system matrix vary as a function of source location, a 4.4 mCi ^{252}Cf was measured at nine different locations, each with a 2-m standoff. The locations were chosen to span a reasonable portion the upper-left quadrant of the FOV (as shown in Figure 11 and Figure 12). Each measurement lasted 15 minutes, which provided enough measured events to generate well converged isolated spectra with a level of statistical uncertainty that would be reasonably achievable in realistic measurement scenarios. A ^{252}Cf source was chosen so that a large energy range for both photons and neutrons could be probed simultaneously. While this strategy introduces energy dependent correlations that are not accounted for in this analysis, it provides a good approximation of the location dependent variance for a photon and neutron energy spectra produced through fission.

Table 2. Total number of measured neutron and photon events at each location and unfolded counts in the corresponding 5×5-pixel ROI. All measurements were performed at a 2-m standoff.

#	Location	Neutrons		Photons	
		Measured Events	ROI Counts	Measured Events	ROI Counts
1	(90°, 90°)	6.35×10^4	1.78×10^8	5.84×10^5	9.86×10^8
2	(110°, 90°)	6.98×10^4	1.93×10^8	6.55×10^5	1.04×10^9
3	(135°, 90°)	5.81×10^4	1.97×10^8	6.26×10^5	1.08×10^9
4	(90°, 65°)	6.91×10^4	1.89×10^8	6.42×10^5	9.53×10^8
5	(110°,65°)	7.04×10^4	1.90×10^8	6.97×10^5	1.03×10^9
6	(135°, 65°)	6.46×10^4	1.97×10^8	7.19×10^5	1.06×10^9
7	(90°, 45°)	5.70×10^4	1.89×10^8	5.69×10^5	8.53×10^8
8	(110°, 45°)	6.04×10^4	1.93×10^8	6.22×10^5	8.37×10^8
9	(135°, 45°)	5.98×10^4	2.00×10^8	6.47×10^5	9.03×10^8

Table 2 summarizes the source locations and number of neutron and photon events measured at each location. Also included in Table 2 are the number of unfolded counts in the 5×5 pixel ROIs centered at each location. These values are equivalent to the integral of the isolated spectra and are the factors used to normalize each spectrum, which allows for a comparison to be made between shapes. Ideally, the ROI counts for each particle would be identical (within the limits of

.

statistical uncertainty) at all locations. However, it is especially clear that the unfolded photon counts for locations 7-9 fall significantly below the unfolded photon counts for locations 1-6. The drop in unfolded photon counts in locations 7-9 is a result of the broadened point-spread function, which is apparent in Figure 12.

Figure 11 and Figure 12 show the neutron and photon images, respectively, as a function of measurement location. The color scale, which represents the number of unfolded counts in a pixel, is fixed (for each particle type) to facilitate comparison between locations. In general, a similar trend can be seen for both photons and neutrons. In all cases, the hot-spot correctly locates the source. However, as the inclination angle is increased, the hot-spots suffer from increased blur. The broadened point-spread function is likely caused by two related factors: the decrease in pixel area as a function of inclination and the associated increase in statistical uncertainty of the associated source-space bins of the system matrix. The photon images show significantly more noise than the neutron images, which is due to the amount of room return and secondary gammas not produced directly by the ^{252}Cf source.

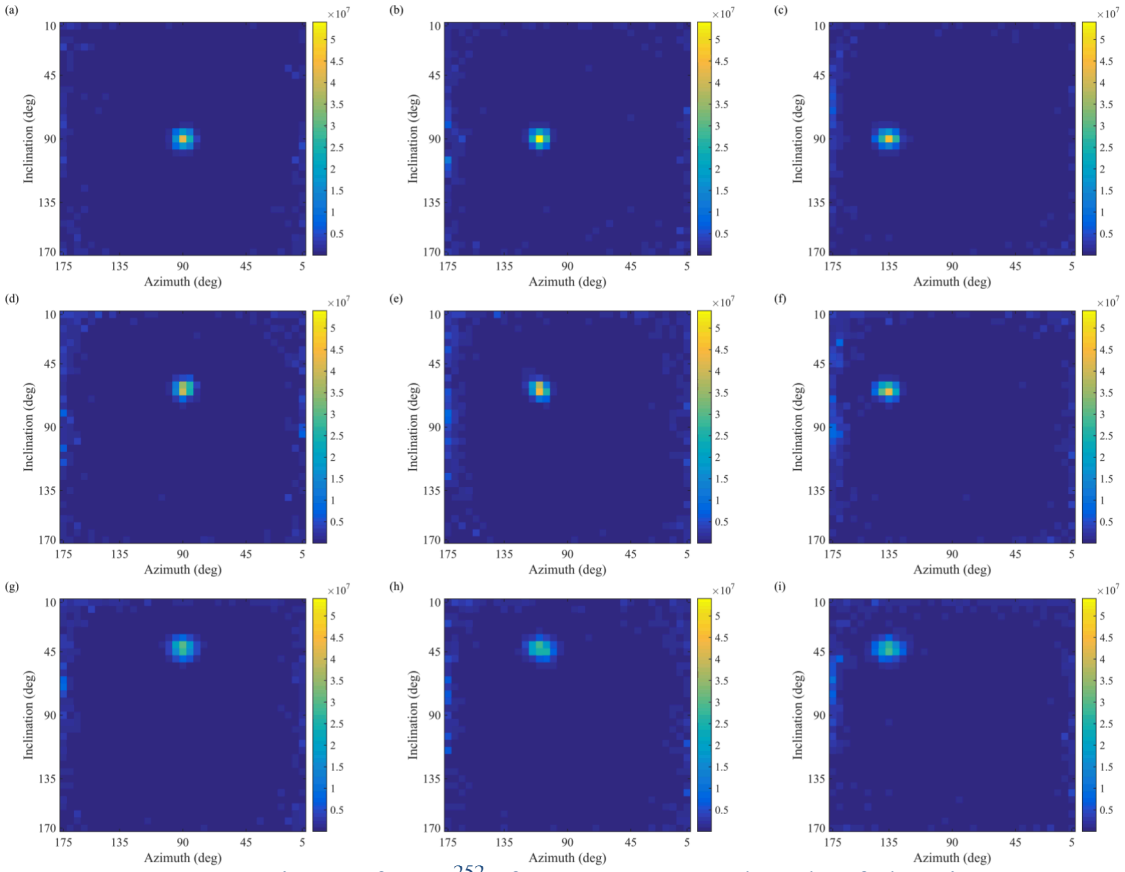

Figure 11. Neutron image for a ^{252}Cf source measured each of the nine source locations summarized in Table 2. The color scale is fixed across all images.

.

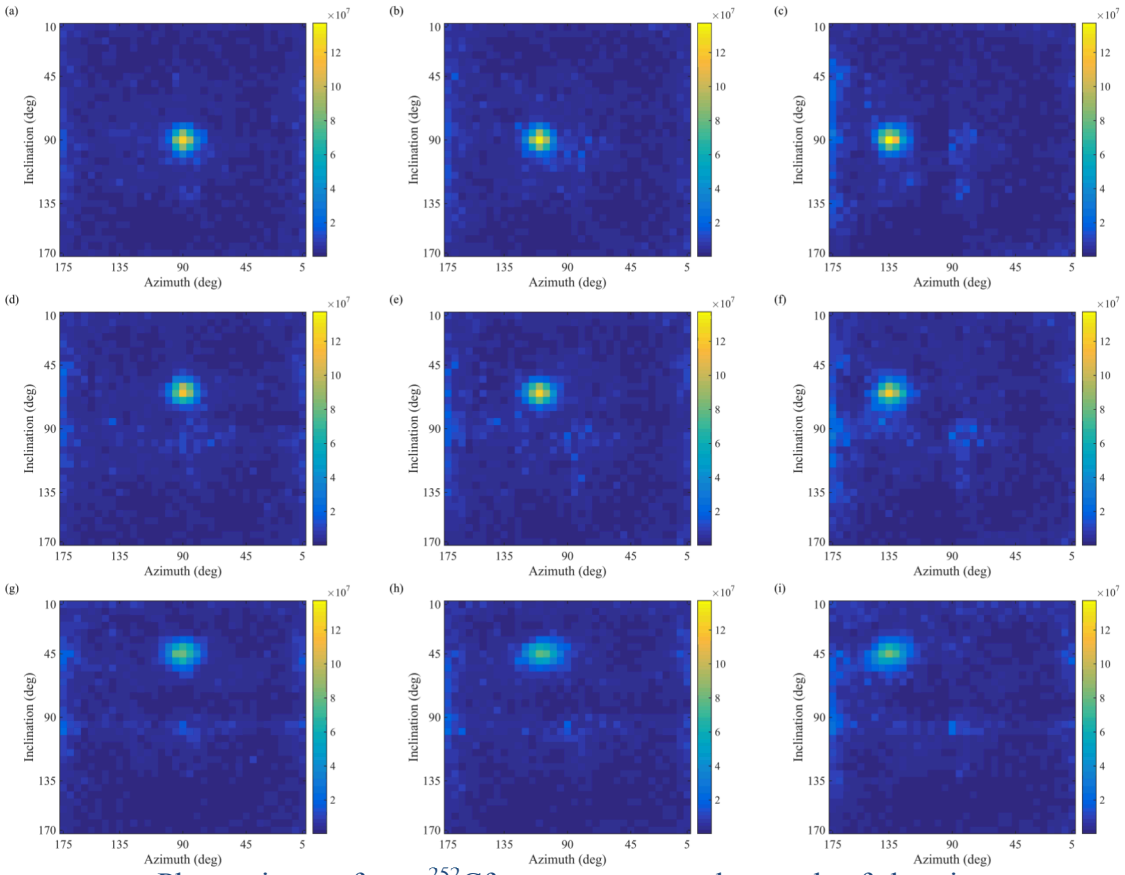

Figure 12. Photon image for a ^{252}Cf source measured at each of the nine source locations summarized in Table 2. The color scale is fixed across all images.

Figure 13 plots the mean neutron (a) and photon (b) spectra across each all 9 measurements. The black circles denote μ_T and the black error bars represent the expected statistical standard deviation, σ_S, for each energy bin. The colored error bars show the observed standard deviation, σ_T. The observed standard deviation is displayed as red when the null hypothesis is rejected and displayed as green when the null hypothesis is accepted (using a false alarm probability of α=0.05). Figure 14 presents the same information in terms of relative uncertainty, where the black circles represent σ_S/μ_T and the colored circles show σ_T/μ_T.

For both particle types, the observed variance in most energy bins was found to be dominated by the expected statistical variance. However, there are a few energy bins in which an additional

.

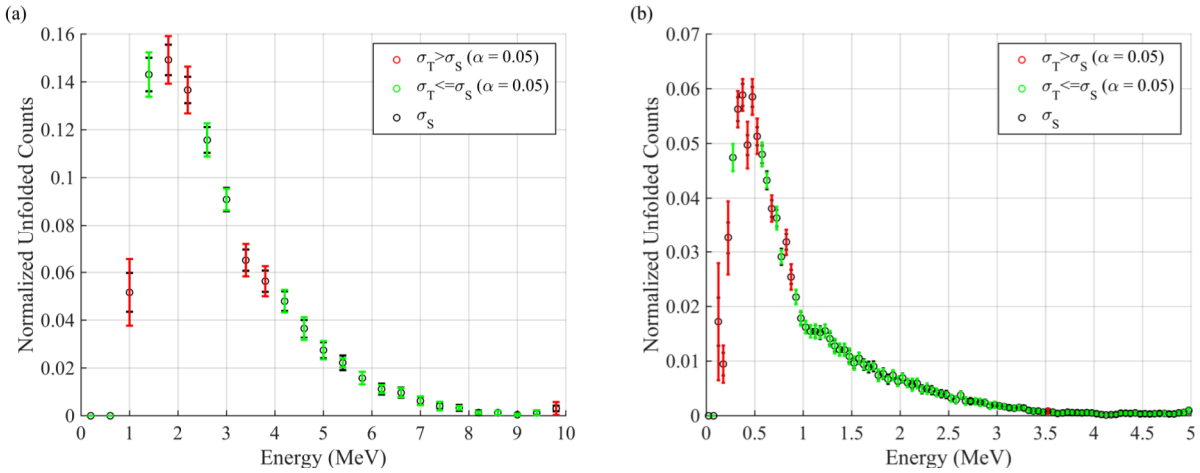

Figure 13. Observed uncertainty, σ_T, (shown as black bars) and expected statistical uncertainty, σ_S, (shown as red or green bars) for each energy bin in the mean neutron (a) and photon (b) spectra. Red bars denote energies in which a systematic uncertainty may have been observed.

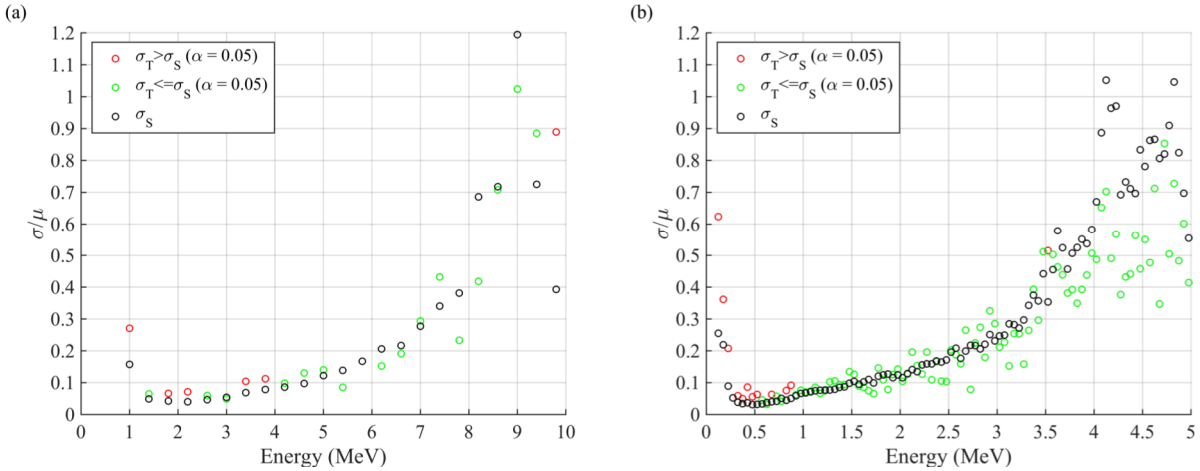

Figure 14. Observed relative uncertainty, σ_T/μ_T, (shown as red or green circles) and expected statistical uncertainty, σ_S/μ_T, (shown as black circles) for each energy bin in the neutron (a) and photon (b) spectra. Red circles denote energies in which a systematic uncertainty may have been observed.

source of uncertainty was detected. With both particles, a large systematic deviation was found in the first bin above threshold, which is not surprising because the first bins suffer from reconstruction noise and are especially subject to room return. Similarly, the highest energy neutron bin also shows a large systematic deviation. However, this bin also suffers from reconstruction noise resulting from neutrons higher than 10 MeV and misclassified particles.

In addition to the edge bins, a systematic deviation was observed at four neutron energy bins. However, both Figure 13 and Figure 14 suggest that the additional variation is relatively small.

.

Recalling that the systematic and statistical components will add in quadrature, it is possible to estimate σ_Q/μ_T to fall between ~5%-8%, which is on the same order as the statistical uncertainty component. This estimate should be taken at face value, because a reliable quantification of the systematic uncertainty would require many more measurements with much lower statistical uncertainty. Nonetheless, it is important to see that systematic uncertainties in the system matrix do not dominate the variation in isolated neutron spectra from one location to another (at least at this level of statistical uncertainty).

For photons, a larger number of bins show an observed systematic deviation. However, with the exception of four bins (.65-.70, 0.80-0.85, 0.85-0.90, and 3.5-3.55 MeV), systematic deviations were only observed in the regions of the spectrum known to be impacted by room return and non-source photons (such as the ^{10}B(n,α) peak in the 0.45-0.50 MeV bin). The contribution of these effects is expected to change with the source location because different locations will place the source at different distances from different scattering surfaces. Considering the number of non-source photons detected, it is not surprising that systematic deviations are observed in these energy ranges. While the presence of these "non-source effects" does not mean that there are no other systematic uncertainties present, it is not possible to distinguish between reconstruction-related and source-related contributions. Nonetheless, the magnitude of these additional deviations is still encouraging. In most cases where a systematic deviation was observed, the total relative uncertainty still remains below 10% including a statistical contribution of ~3-5%. There is a single spurious point of observed systematic deviation that occurs in the 3.5-3.55 MeV bin, however, this is likely a result of a large fluctuations seen in the estimated statistical uncertainty component in this region.

The results of this study show that the shape of the isolated photon and neutron spectra compare reasonably well across different locations in the FOV. Some systematic uncertainties were observed, but their impact was small and would not be expected to significantly impact the ability to characterize a detected source based on the shape of the isolated spectra. This study probed a large portion of the system matrix, and the lack of gross systematic variations speaks to the robustness of the simulation technique used to compute the system matrix.

While a much deeper analysis is required to determine the exact source of the observed systematic uncertainties, it is easy to speculate as to what the largest contributing factors might be. As the location of the source changes the scattering angle between a specific detector pair also changes. As a result, different reconstructed energy ranges will be impacted by uncertainties associated with the modeled resolution and light-output functions (for neutrons), especially at low energy depositions. Additionally, as the source is moved away from (90°, 90°), incident particles will be less likely to interact in the front plane PMTs, which reduces the impact of any model mismatch present in the PMT model.

RESULTS:

.

The previous section described the measurement system and data processing methodology that is capable of locating and characterizing photon and neutron sources using a combination of imaging and localized spectroscopy. We demonstrated the utility of the spectrum-isolation method for analyzing both source and non-source locations to obtain the most information available about the environment being investigated and demonstrated that the shapes of isolated spectra can be reliably compared across different source locations and standoff distances. These results suggest that the combination of the DPI and the spectrum-isolation technique form a powerful tool for detecting, localizing, and characterizing radioactive materials and is particularly well suited for identifying SNM.

In this section we test these claims by presenting a complex measurement scenario involving SNM, multiple sources, and shielding. The results presented will show that the DPI is capable of localizing and characterizing all radioactive sources in these experiments. An in-depth analysis of the isolated photon and neutron spectra will show that not only can the radioactive material be identified using their characteristic signatures, but also that some determinations can be made regarding the presence and nature of shielding material.

Identifying Weapons-Grade Plutonium

In July 2015, the DPI was taken to the Device Assembly Facility at the Nevada National Security Site to measure various samples of category-I SNM. One such sample available for measurement was the Thor Core– a 4.1-kg disc of WGPu. The following section will be used to discuss one experiment involving the Thor Core that is particularly applicable to several non-proliferation applications including treaty verification, emergency response, and active facilities monitoring.

The Thor Core

The Thor Core[32] is a 4.1-kg disc of weapons grade plutonium (WGPu), which qualifies it as category-I strategic SNM. Figure 15 gives the dimensions of the sample as reported by [33]. Table 3 details the plutonium composition of the sample based off the values quoted in 1972. Due to the relatively short half-life of ^{241}Pu ($T_{1/2}$=14.29 years), these values should be adjusted for the buildup of ^{241}Am, which is produced through the β-decay of ^{241}Pu with a branching ratio of 99.99%, and will have discernable gamma-ray signatures. Table 4 makes this adjustment, while ignoring the negligible loss of ^{239}Pu ($T_{1/2}=2.41\times10^4$ years) and ^{240}Pu ($T_{1/2}=6.56\times10^3$ years). The balance of the ^{241}Pu branching ratio yields an α decay to ^{237}U. The very short half-life ($T_{1/2}$=6.75 days) of ^{237}U results secular equilibrium with ^{241}Pu, which allows for the strong gamma rays of ^{237}U to be associated with ^{241}Pu.

[32] The term "Thor Core" is used to reference the middle piece of the full Thor Core, which is the only piece that was made available for measurement. The full Thor Core is a three-piece subcritical plutonium assembly operated by Los Alamos National Laboratory[118], [120].
[33] R. B. Kidman, "Reckoning THOR," 1972
.

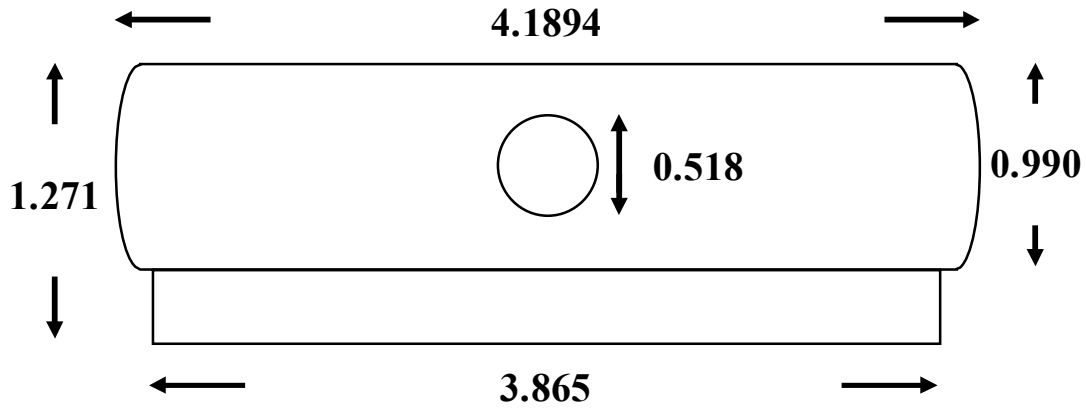

Figure 15. Diagram of the Thor Core with dimensions given in inches.

Table 3. Thor Core plutonium composition by isotope circa 1972.

Isotope	Atom %	Mass (g)
^{239}Pu	94.66	3867.69
^{240}Pu	5.02	205.11
^{241}Pu	0.32	13.07
Total:	100.00	4085.87

Table 4. Expected 2015 Thor Core composition by isotope.

Isotope	Mass (g)
^{239}Pu	3867.69
^{240}Pu	205.11
^{241}Pu	1.64
^{241}Am	11.43
Total:	4085.87

As a plutonium metal sample, the neutron energy spectrum will be well approximated by the Watt fission spectrum. Table 5 lists the prominent gammas signatures between 0.3 and 0.8 MeV expected from the Thor Core. While not listed in this Table 5, ^{241}Am has several strong decay gammas below 0.3 MeV, the most notable of which is the 0.059 MeV gamma ray emitted by ^{241}Am at a rate of 4.54×10^{10} γ/s-g. The intensity of these gammas necessitated the use of an increased threshold in the NaI(Tl) detectors (~0.25 MeV) to prevent saturation of the data-acquisition system. The increased threshold results in a minimum detectable photon energy of approximately 0.29 MeV.

.

Table 5. Prominent gamma signatures expected from the Thor Core.

^{239}Pu		^{240}Pu		^{241}Pu [α]		^{241}Am	
Energy (MeV)	**γ/s-g**	**Energy (MeV)**	**γ/s-g**	**Energy (MeV)**	**γ/s-g**	**Energy (MeV)**	**γ/s-g**
0.345	1.28×10^{4}	0.642	1.05×10^{3}	[α] 0.332	1.14×10^{6}	0.335	6.28×10^{5}
0.375	3.60×10^{4}			[α] 0.371	1.04×10^{5}	0.662	4.61×10^{5}
0.413	3.42×10^{4}					0.722	2.48×10^{5}
0.645	3.42×10^{2}						
0.717	6.29×10^{1}						

[α] The listed ^{241}Pu signatures come ^{237}U decay, which is in secular equilibrium with ^{241}Pu.

Experiment

An ~850-minute measurement was taken with three neutron-emitting sources present in the FOV: the Thor Core, ^{252}Cf and ^{241}AmBe. Each source was located at a standoff of approximately 2.0 m and lead shielding was used to reduce the ^{241}Am photon flux coming from the Thor Core and ^{241}AmBe source. The location, standoff, shielding, and approximate neutron emission rate for each of these three sources is summarized in Table 6.

Table 6. Source location, approximate neutron emission rate, and shielding for each of the three sources in the FOV.

Source	n/s	Location	Standoff (m)	Shielding
Thor Core	$\sim7.9\times10^{5}$	(90°, 85°)	2.00	1.27-cm Lead
^{252}Cf	$\sim3.0\times10^{5}$	(90°, 110°)	2.11	None
^{241}AmBe	$\sim1.0\times10^{6}$	(141°, 85°)	2.07	10-cm Lead

Approximately 1.6×10^{5} neutron events and 1.0×10^{6} photon events were acquired. The high number of photon events acquired facilitated the use of a 0.025 MeV source-space energy bins in the photon system matrix, rather than the 0.050 MeV bins that have been used throughout this work.

.

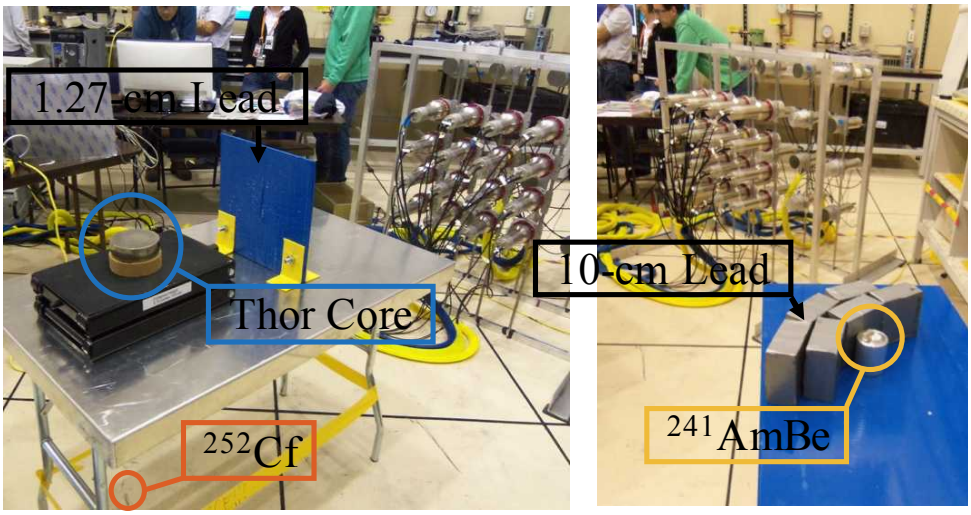

Figure 16. Photographs of the experimental setup. The Thor Core is located at (2.00 m, 90°, 85°) behind a 1.27-cm thick lead shadow-shield. The ^{252}Cf is located 4.5 cm above the floor directly below the Thor Core at (2.11 m, 90°, 110°). The ^{241}AmBe is located at (2.07 m, 141°, 85°) behind approximately 10 cm of lead shielding.

Figure 16 shows two photographs of the experimental setup. The Thor Core was oriented such that the flat sides of the disc were parallel to the floor, which was a safety precaution to prevent the source from tipping over during the unattended overnight measurement. The ^{252}Cf source was placed 4.5 cm above the floor, directly below the Thor Core. The ^{241}AmBe source was placed on a table to the left of the Thor Core (from the perspective of the DPI). The Thor Core was shielded by a 1.27-cm thick lead shadow-shield and the ^{241}AmBe source was shielded by 10 cm of lead bricks.

It is worth noting that while the expected gross neutron emission rate (reported in Table 6) for the Thor Core can be reasonably well estimated, the apparent emission rate observed by the DPI is affected by the orientation of the sample. Simulations have shown that the flat orientation used in this experiment results in a count rate that is ~63% lower than the neutron count rate detected using a face-on orientation. The reduction in measured count rate is a consequence of self-shielding caused by the size and mass of the sample. Additionally, the observed emission rates of both the Thor Core and ^{241}AmBe source will be reduced by the lead shielding.

Results

Figure 17 shows the reconstructed neutron and photon images. While the neutron image shows three hot-spots all centered in the correct pixels, the photon image only locates two of the three sources (also at the correct location). The ^{241}AmBe hot-spot is absent, due to the significant amount of lead shielding present around the source. While the absence of the ^{241}AmBe photon

.

hot-spot may be initially seen as a failure (and in some sense it is), there is an important piece of information to be learned from this. Neutron-emitting materials are expected to be accompanied by photons, and therefore, a corresponding photon hot-spot is expected for every neutron hot-spot. As such, the absence of a corresponding photon hot-spot is a signal that high-Z material may be present. While the presence of lead was known *a priori* in this measurement, the ability to obtain such information is important when investigating an unknown environment. It is worth pointing out that a photon-only detector of similar sensitivity would potentially be blind to the presence of the ^{241}AmBe source, which highlights a benefit of dual-particle sensitivity.
Figure 18 shows, for both photons and neutrons, a direct comparison between the isolated spectra from each of the three ROIs shown in Figure 17. There are obvious differences in both the photon and neutron spectra for all three sources, which are discussed in greater detail over the following pages.

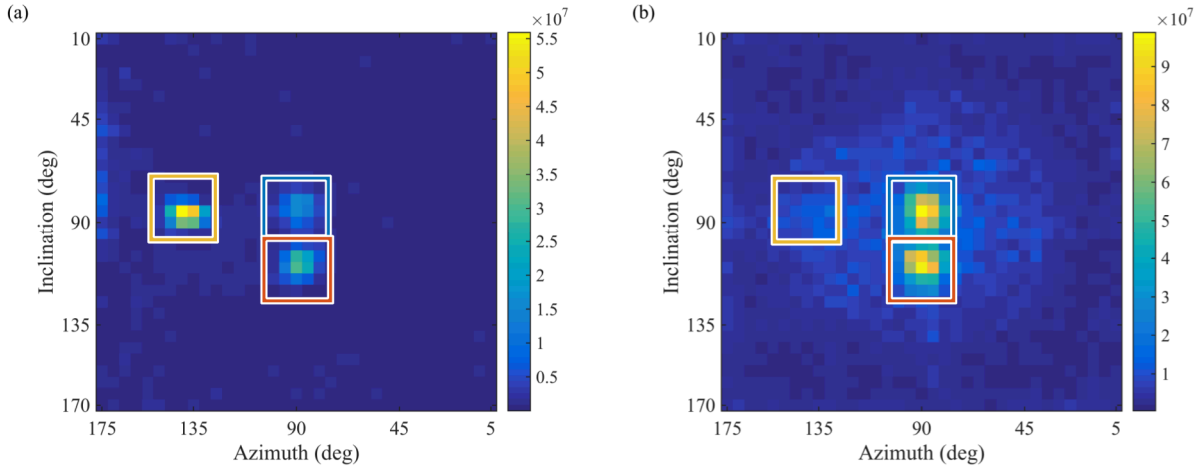

Figure 17. Reconstructed neutron (a) and photon (b) images. Neutron image correctly locates all three sources while photon image correctly locates the Thor Core and the ^{252}Cf. The ^{241}AmBe hot-spot is absent from the photon image due to heavy lead shielding. Colored boxes denote the 5×5-pixel ROIs used to generate the isolated spectra shown in Figure 18.

.

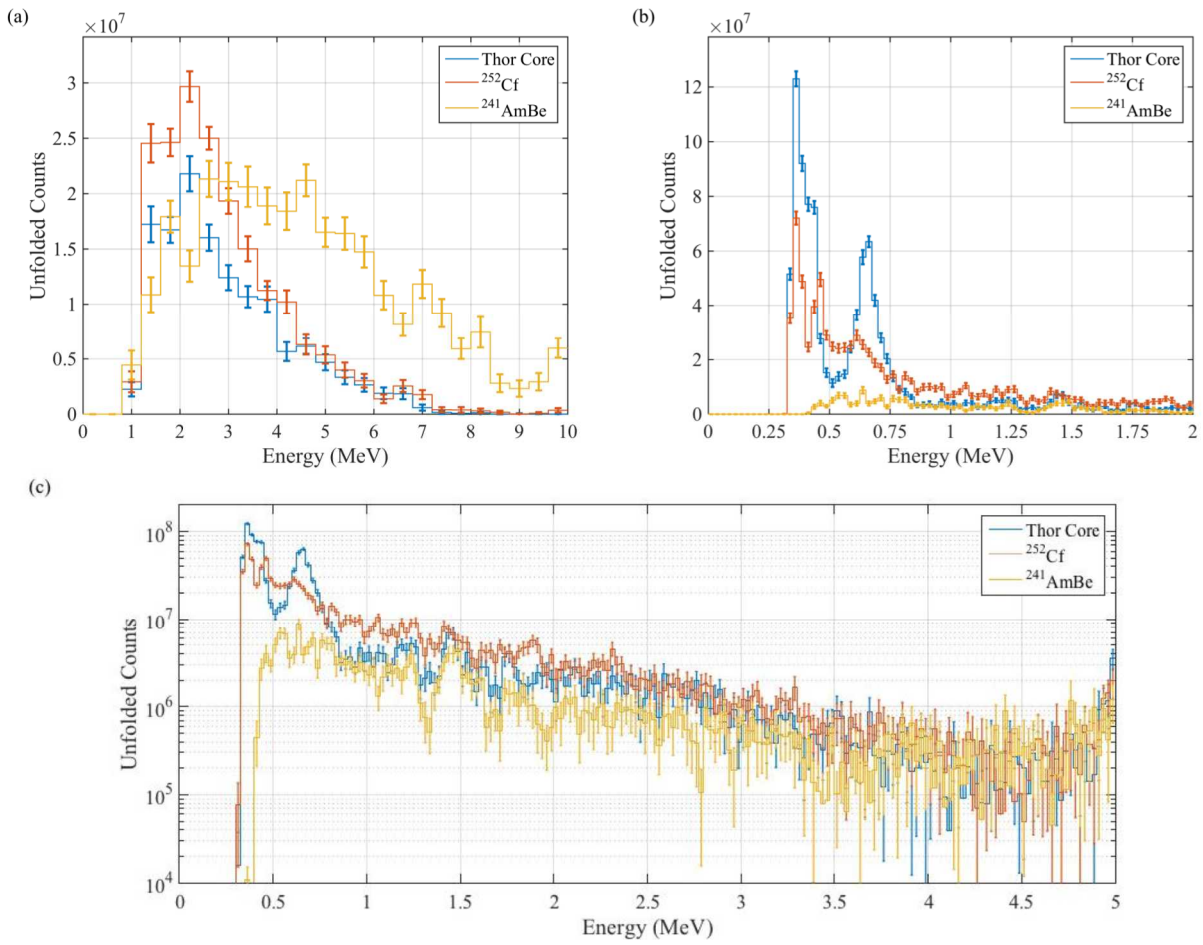

Figure 18. Isolated neutron (a) and photon (b), (c) corresponding to the 5×5-pixel ROIs shown in Figure 17. The photon spectra are shown on a linear scale over a reduced energy range in (b) and on a logarithmic scale over the full range in (c). Error bars represent $\pm 1\sigma$.

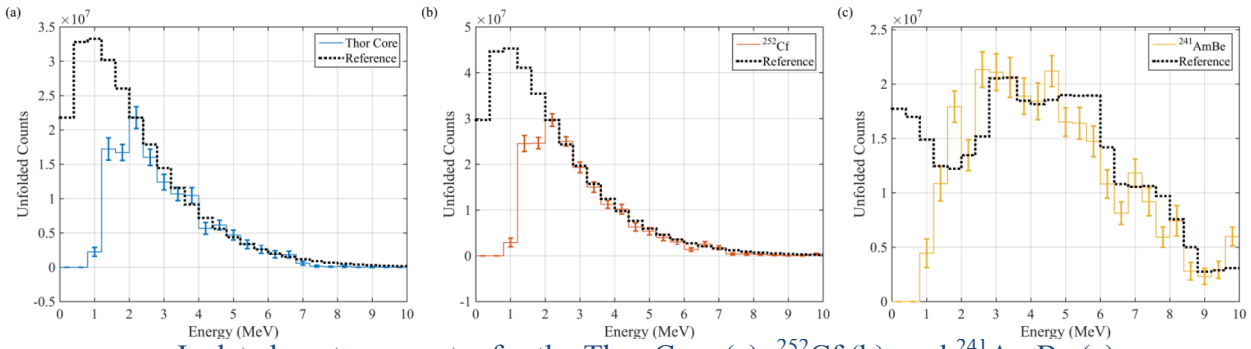

Figure 19. Isolated neutron spectra for the Thor Core (a), ^{252}Cf (b), and ^{241}AmBe (c) ROIs shown in Figure 17. The reference spectrum in (a) and (b) is the theoretical ^{252}Cf spectrum and the reference spectrum in (c) is the theoretical ^{241}AmBe spectrum. All reference spectra are scaled to match the intensity of the corresponding isolated spectrum in the 2.0-2.4 MeV energy bin. Error bars represent $\pm 1\sigma$.

Figure 19 shows how each of the isolated neutron spectra compare to corresponding reference spectra. Both fission sources are compared to the ^{52}Cf reference spectrum to emphasize the similarities in the neutron spectra between the two sources. In all cases the reference spectra are scaled to match the intensity of the measured spectrum in the 2.0-2.4 MeV energy bin. Acknowledging the expected variation in ^{9}Be(α, n) spectra, it is clear that all three spectra compare well to their references for energies above ~2 MeV. Both the Thor Core and the ^{252}Cf agree especially well, with the reference spectrum falling within the estimated uncertainty in almost all energy bins.

The neutron spectra alone facilitate discrimination between ^{9}Be(α, n) source and the fission sources. However, the neutron spectra do not allow for the Thor Core to be distinguished from the ^{252}Cf due to the similarities in the neutron energy distribution across fission sources. Fortunately, the availability of localized photon spectra makes this discrimination possible. It is apparent in Figure 19 (b) and (c) that the isolated photon spectra for these two sources are very different and the forthcoming analysis will demonstrate that the spectral features are well aligned with the expected features of each source.

.

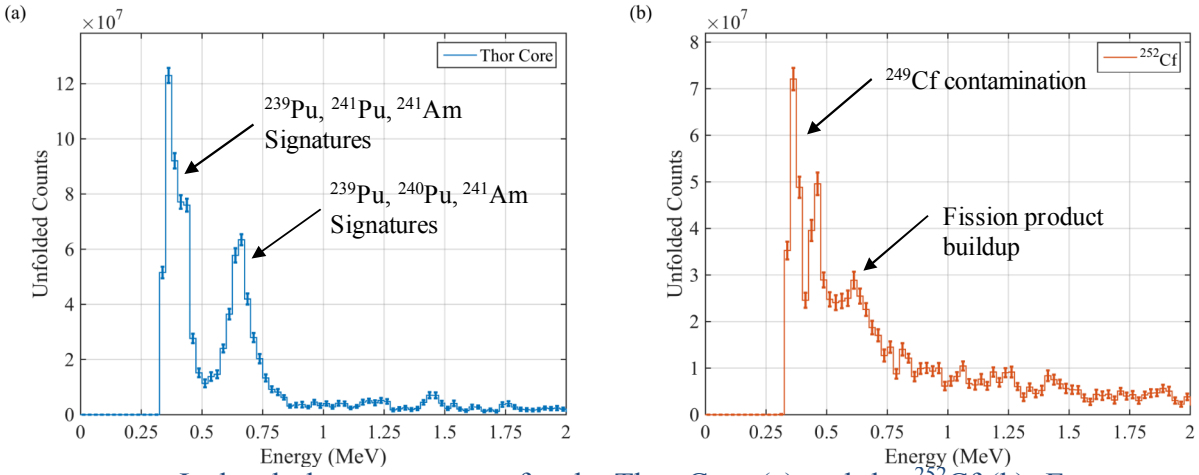

Figure 20. Isolated photon spectrum for the Thor Core (a) and the ^{252}Cf (b). Error bars represent $\pm 1\sigma$.

Figure 20 highlights the notable features of the isolated photon spectra for the Thor Core and the ^{252}Cf source. The Thor Core spectrum is dominated by two peaks located in the 0.300-0.475 MeV energy bins and the 0.550-0.750 MeV energy bins. While the DPI does not have the requisite resolution to individually resolve the individual emission lines of the Thor Core, it is clear that these peaks are well aligned with the energy ranges outlined in Table 5.

The ^{252}Cf spectrum appears to have more of a continuum than the Thor Core spectrum (which is seen more clearly in Figure 19 (b) and (c)). On top of this continuum are three prominent features. The peak between 0.350 and 0.400 MeV and the protrusion in the 0.650 MeV range are due to the age of the source[34]. The third feature is the peak located in the 0.425-0.475 MeV energy bins, which is tentatively left as unidentified.

The age-related features in the ^{252}Cf spectrum appear at similar energies as the expected plutonium signatures, which makes it more difficult to discriminate between the two fission sources. However, the overall shape of the spectra makes discrimination between the two fission sources possible. It is worth noting that the difference in shape would be even more apparent if ^{252}Cf source were newer.

It is possible that the unidentified feature is related to the 0.478 MeV ^{10}B(n,α) feature seen in previously discussed experiments performed in the standard laboratory space. The DAF facility provided a much larger measurement space and the total neutron emission rate in this measurement (~2.1×10^6 n/s) is an order of magnitude lower than the neutron emission rate of the previously measured 4.4 mCi ^{252}Cf source (~1.9×10^7 n/s). These factors should both result in a

[34] R. . Gehrke, R. Aryaeinejad, J. . Hartwell, W. . Yoon, E. Reber, and J. . Davidson, "The γ-ray spectrum of 252Cf and the information contained within it," *Nucl. Instruments Methods Phys. Res. Sect. B Beam Interact. with Mater. Atoms*, vol. 213, pp. 10–21, Jan. 2004

.

lower rate of thermalized neutrons incident on the DPI, and therefore a lower $^{10}B(n,\alpha)$ signal. However, in this particular experiment, the two fission sources were located directly between the DPI and the Fast-Neutron Coded-Aperture Imager[35], which was deployed with a large borated-polyethylene mask. As such, it is possible that the DPI is also detecting $^{10}B(n,\alpha)$ gammas being emitted by the mask. If this theory is correct, a similar signal would also be expected in the Thor Core ROI. However, it is difficult to determine if such a signal is present because the relevant energy bins are contained within the low-energy peak of the isolated Thor Core spectrum.

Figure 21 shows a comparison between the isolated photon spectrum of the ^{241}AmBe ROI and a 5×5-pixel "background" ROI taken from a similar location, (40°, 85°), on the opposite side of the image. The ^{241}AmBe spectrum shows considerable overlap with the background spectrum. It is clear that there is no surplus signal in the 4.4 MeV region, which would have been the most likely gamma energy to pass through the 10 cm of lead shielding.

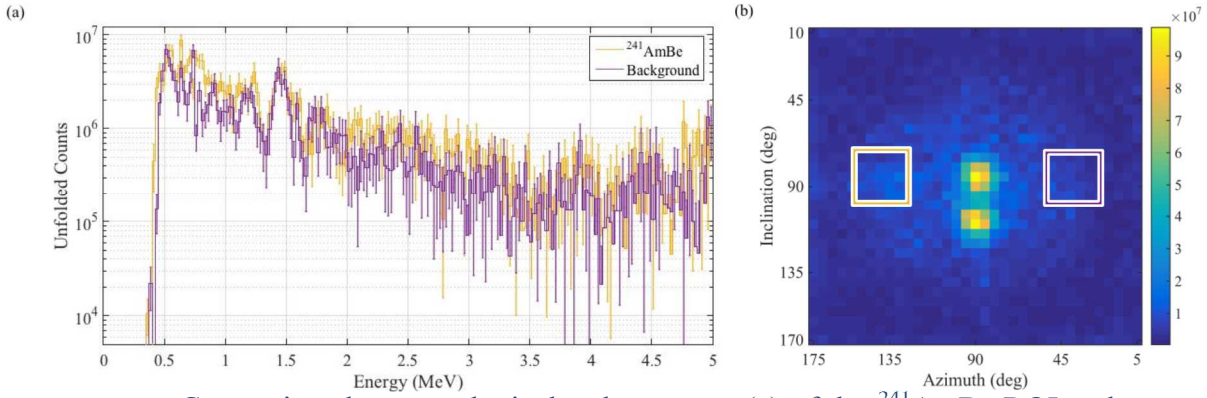

Figure 21. Comparison between the isolated spectrum (a) of the ^{241}AmBe ROI and the background ROI denoted by the purple box in (b). Error bars represent $\pm 1\,\sigma$.

DISCUSSION:

The results presented in the last section demonstrate how the DPI was used to successfully locate a category-I SNM sample from a field of three neutron-emitting sources. The success of this experiment was highly dependent on the localized spectroscopy capabilities provided by the spectrum-isolation technique. In addition to locating the SNM sample, the four data-pathways of the DPI were used in various combinations to draw several other conclusions, which are summarized in Table 7. While no claims are made on the minimum time (or measured events) required to draw these conclusions, the small relative error associated with the isolated spectra suggests that the full 850-minute data set is not required.

[35] P. Hausladen, J. Newby, F. Liang, and M. Blackston, "The Deployable Fast-Neutron Coded- Aperture Imager : Demonstration of Locating One or More Sources in Three Dimensions Prepared by," 2013

.

Table 7. Summary of conclusions drawn and the data pathways used to facilitate them.

Conclusion	Neutron Image	Neutron Spectrum	Photon Image	Photon Spectrum	Details
3 neutron sources at (90°, 85°), (90°, 110°), and (140°, 85°)	X				Three hot-spots identified in neutron image.
2 fission sources at (90°, 85°) and (90°, 110°)	X	X			Localized neutron spectra compare well with Watt distribution.
1 non-fissile fission source located at (70°, 90°)	X	X	X	X	Localized neutron spectrum compares well with Watt distribution. Absence of characteristic decay gammas expected from fissile sources.
1 plutonium sample (SNM) located at (90°, 85°)	X	X	X	X	Localized neutron spectrum compares well with Watt distribution. Localized photon spectrum decay lines consistent with plutonium.
1 ^{9}Be(α, n) source at (140°, 85°)	X	X			Localized neutron spectrum compares well with ^{241}AmBe spectrum.
^{9}Be(α, n) shielded by high-Z material present at (140°, 85°)	X	X	X	X	3 neutron hot-spots but only 2 photon hot-spots. Localized photon spectrum compares well with background estimate.

.

Many of the conclusions drawn from these experiments could also be drawn independently from the use of several, less versatile systems. However, one of the greatest advantages of the DPI is the ability to provide four synchronized data-pathways. These four pathways allow for the user

.

to cross-reference localized photon and neutron data obtained concurrently from a single system, which is particularly advantageous in applications concerning the detection of SNM.

ANTICIPATED IMPACT:

The proposed research will help to advance imaging detectors such as the University of Michigan Dual Gamma/Neutron Imager, and SNL's Neutron Scatter Camera and Coded Aperture Imagers from qualitative imaging to quantitative measurement devices. The imaging and analysis capability to be developed is of interest to Office of Nuclear Verification and to the Fuel Cycle R&D program. The technology is potentially of interest to NA-42 for diagnostic neutron imaging as well as DHS and DTRA in that it can be scaled to large areas to search for SNM neutron sources either passively or in support of active interrogation scenarios.

At many points throughout this work attention was drawn to open challenges and avenues for future improvement. Admittedly, much of the analysis presented in this work was performed from a qualitative standpoint. However, the groundwork has been laid to move in the direction of more quantitative analysis. The viability of bootstrapping allows for detailed statistical analysis to automate detection and characterization. The implementation of such algorithms may improve the sensitivity of the system by removing the need to obtain "well-converged" spectra.

Additionally, with further work, accurate and reliable estimates of ROI intensity could enable the determination of characteristics such as the absolute activity and fissile mass. In prior work we have demonstrated that the 5×5-pixel ROIs under-predicted the expected source strength. Furthermore, the under-prediction was not found to be consistent between different sources or different energies. With a better understanding of the influential factors, it may be possible to correct the under-prediction. This approach would open up the possibility of estimating the source strength of detected materials at a known distance. Furthermore, these corrections are likely to be of different strength for gammas and neutrons. If corrected, the absolute neutron to gamma ratio could be used to make further inferences on the size and shape of the detected objects.

In the previous section, some allusions were made to the possibility of characterizing intervening materials by comparing the attenuated spectra to suspected material cross sections. Such an analysis could yield information on both the properties and thicknesses of the intervening material, which could be used to estimate source strength of shielded nuclear material. The ability to accurately estimate uncertainty in the isolated spectra, such as through the use of the bootstrapping technique, is a necessary first step towards this goal. Knowing the uncertainty in the isolated spectra makes it possible to determine if deviations from an expected reference spectrum are within the statistical limitations of the measurement or if they are the result of attenuation by an intervening material. If an intervening material is detected, then the estimated uncertainties in the spectrum could be used to estimate the uncertainty on the calculated

.

thickness of the intervening material. It is worth noting that this effort would benefit greatly from improvements to the energy resolution of the DPI.

Each of the above endeavors would benefit from further understanding of the statistical and systematic uncertainties associated with the system matrix. Several potential sources of model mismatch were alluded to and many warrant a more in-depth analysis than was afforded in this work. Features such as the flat top on the Watt distribution seemed to be fairly consistent and could likely be corrected for by including some estimate of PSD misclassification in the system matrix. The effect of statistical uncertainties within the system matrix itself were not considered in this work and should be studied further. The use of bootstrapping to estimate the statistical uncertainties of the system matrix may help provide a more comprehensive estimate of the statistical contributions to uncertainty in spectrum-isolation solutions. Additionally, the analytic noise-propagation models that have been developed for tomographic image reconstruction may be useful for further characterizing uncertainty in the spectrum-isolation solutions [36, 37,38.] Models related to system matrix error would be especially useful because they can provide insight into the level of accuracy needed in the system matrix computation to achieve a desired level of uncertainty in the solutions.

The system matrix itself also offers several avenues for improvement. Implementing a more optimal binning structure might include a strategic change of basis or even a full re-parameterization of the problem. Improvements could also be made to the accuracy of the overall model. Such work might include further improvement of the light-to-energy conversion and resolution functions, as well as the addition of new capabilities, such as the simulation of full light propagation and simulated pulse-shape discrimination. Efforts could be made to reduce the computation time required to simulate the system matrix. In addition to leveraging the previously mentioned analytic noise-propagation models, computation time could be reduced by strategically finding and removing less relevant regions of the model. Additionally, it may be possible to simulate fewer source space bins and simply interpolate to finer resolutions. Although well developed, the DPI certainly has room for improvement. We have shown that the spatial resolution of individual interactions limited the achievable angular resolution for both photons and neutrons the energy resolution of neutrons. Spatial resolution could be improved by using smaller detector cells, using pixelated read-outs (such as SiPMs), or simply moving the detectors further apart. The SiPM route is the most interesting because it would also result in a more compact form-factor and would not inherently reduce the efficiency. It would also be possible to improve photon energy resolution by using higher resolution materials including, but not limited to, CsI, $LaBr_3$, or CdZnTe. However, due to the summation of front and back plane energy depositions, these improvements would be tempered by the lower resolution of the EJ-

[36] D. W. Wilson, B. M. W. Tsui, and H. H. Barrett, "Noise properties of the EM algorithm. II. Monte Carlo simulations," *Phys. Med. Biol.*, vol. 39, no. 5, pp. 847–871, May 1994
[37] J. Qi and R. H. Huesman, "Propagation of Errors From the Sensitivity Image in List Mode Reconstruction," *IEEE Trans. Med. Imaging*, vol. 23, no. 9, pp. 1094–1099, Sep. 2004
[38] J. Qi and R. H. Huesman, "Effect of errors in the system matrix on maximum a posteriori image reconstruction," *Phys. Med. Biol.*, vol. 50, no. 14, pp. 3297–3312, Jul. 2005.
.

309 detectors. Additionally, improvements could be made in the pulse-shape discrimination capabilities of the scattering detectors by moving to a material such as stilbene.

CONCLUSION:

Several non-proliferation and treaty verification applications may benefit from robust radiation imaging techniques. These applications rely on the ability to accurately detect, localize, and characterize radioactive materials, specifically SNM. The goal of this work was to develop powerful data-processing algorithms that are able to reliably meet these needs.

We have developed and implemented such algorithms on the DPI, as a versatile detection system capable of providing data through four main pathways:

1. Neutron imaging
2. Photon imaging
3. Neutron spectroscopy
4. Photon spectroscopy

We have introduced and explored the use of the spectrum-isolation technique, which is an image and spectrum reconstruction algorithm designed to extract information from these four pathways. We have relied on Monte Carlo simulation techniques to compute the detailed system matrix that makes the spectrum-isolation technique successful.

Having established the utility of the spectrum-isolation technique, we worked to determine the uncertainty associated with the reconstructed solutions and demonstrated that a bootstrapping technique could be used to reliably estimate statistical uncertainties using only a single measurement. Knowing the expected statistical deviations allows for the quantitative assessment of the systematic uncertainties within the system matrix. These uncertainties were investigated through the comparison of isolated spectra generated from the same source measured at a variety of locations and standoff distances. This comparison showed that while the magnitudes of the isolated spectra displayed some variations over the cases investigated, the normalized shapes of the isolated spectra were well aligned across all measurements. This conclusion is an important one because it implies that template matching can be used to compare measured spectra to expected distributions and draw concrete conclusions on any observed deviations – beyond those predicted by statistical uncertainty.

As a final proof of concept, we analyzed data taken from a very complex environment, relevant to non-proliferation, using the methods outlined in this work. The DPI was able to successfully locate and identify the SNM sample in this cluttered environment. A 4.1 kg WGPu sample (classified as category-I SNM) was identified in a FOV that also contained a ^{252}Cf source and a lead-shielded ^{241}AmBe source. The non-SNM sources were also correctly located and identified and the presence of lead shielding was determined by the absence of a photon signal from the known ^{241}AmBe location. The depth of the conclusions drawn from these final experiments truly

.

demonstrate the contributions of this work towards the established need of reliably detecting, localizing, and characterizing special nuclear materials.

.